Interaction between the helical vortices shed by contra-rotating propellers ⊕

A. Posa ✉ ⓘ ; A. Capone ⓘ ; F. Alves Pereira ⓘ ; F. Di Felice ⓘ ; R. Broglia ⓘ

🔵 Check for updates

△ AIP Publishing

Interaction between the helical vortices shed by contra-rotating propellers 🄴🄿

View Online   Export Citation   CrossMark

A. Posa,[a)] 🄳 A. Capone, 🄳 F. Alves Pereira, 🄳 F. Di Felice, 🄳 and R. Broglia 🄳

AFFILIATIONS

CNR-INM, Institute of Marine Engineering, National Research Council of Italy, Via di Vallerano 139, 00128 Roma, Italy

[a)]Author to whom correspondence should be addressed: antonio.posa@cnr.it

ABSTRACT

Large eddy simulation is adopted to analyze the interaction between the tip vortices shed by two contra-rotating propellers, by using a computational grid consisting of 4.6×10^9 points. Despite the complexity of the wake topology, the results of the computations show an excellent agreement with the measurements from an earlier experimental study on the same system. The interaction between the tip vortices shed by the two propellers produces vortex rings. Each of them consists of six helical sides, which are connected by U-shaped vortex lobes. The three upstream lobes of each vortex ring move to outer radial coordinates, as a result of their shear with the downstream lobes of the upstream vortex ring. In contrast, the downstream U-shaped lobes move to inner radial coordinates, as a result of their shear with the upstream lobes of the downstream vortex ring. This interaction results in an overall expansion of the wake of the contra-rotating propellers. The regions of shear between the U-shaped lobes of consecutive vortex rings are the areas of the largest turbulent stresses, which achieve higher levels than those produced in the wake of the two front and rear propellers working alone. This complex flow physics also triggers a faster instability of the wake system, breaking its coherence at more upstream coordinates, in comparison with the isolated propellers.

I. INTRODUCTION

The efficiency of marine propulsion is of paramount importance for its economic and environmental impact. Contra-rotating propellers are targeted at achieving improved propulsion efficiency. The action of a propeller on the flow results in its acceleration in both axial and tangential directions. The tangential momentum gained by the flow is actually an energy loss, which is not exploited to produce thrust, but it is actually the source of unwanted lateral loads on the system. Contra-rotating propellers are aimed at recovering the tangential momentum transferred by the front propeller on the flow, by using a rear propeller rotating in the opposite direction. Despite the potential advantages of contra-rotating systems, their flow physics is less understood, in comparison with that of more conventional propulsion systems, due to its increased complexity.

To date, most studies on contra-rotating propellers are focused on the analysis of the global performance for improved efficiency and design,[1–11] while little is known about their wake features. While the latter are already especially complex in the case of propellers working alone,[12–23] the analysis of their physics becomes even more problematic, when two contra-rotating propellers work together. Therefore, a very limited number of studies tackle the problem of the wake flow of

contra-rotating propellers, due to the challenge they represent to both experimental and numerical methodologies.

In this context, the most advanced experimental works were recently reported by Capone and co-workers,[24–26] where particle imaging velocimetry (PIV) was adopted to analyze the interaction of the helical vortices. Also, high-speed visualizations were utilized to capture the complex mutual inductance between tip vortices. Their interaction was found to be a strong function of the relative azimuthal position between propellers. The interplay between tip vortices resulted in earlier instability phenomena, following the onset of isolated vortex rings, which were first identified and reported by Capone and Alves Pereira.[24] To the authors' knowledge, no other studies have analyzed experimentally the wake flow of contra-rotating marine propellers with such level of detail of the topology of the tip vortices they shed.

A few numerical works addressing the characterization of the wake flow and in particular the interaction of the tip vortices of contra-rotating propellers are also available. Paik *et al.*[27] studied a similar propulsion system using both Reynolds-averaged Navier–Stokes (RANS) computations and Stereo PIV measurements. About 3×10^6 cells were adopted on the finest grid utilized to reproduce the flow problem. The numerical predictions were validated against the PIV

measurements. The tip vortices shed by the rear propeller were found reinforced by their interaction with those from the front propeller. RANS was also exploited by Huang et al.[28] to reproduce the wake profiles of an underwater vehicle, using a computational mesh consisting of about 5×10^6 cells, but relying on a body force approach to represent the action on the flow by both front and rear propellers at its tail. Therefore, no details were captured on the topology of the tip vortices typically shed by marine propellers.

A more advanced approach was utilized in the work by Zhang et al.,[29] where improved delayed detached eddy simulation (IDDES) allowed reproducing the tip vortices shed by contra-rotating propellers. In this work, the complexity of the wake flow was enhanced by its interaction with a downstream rudder. The front and rear propellers were simulated also operating alone. A grid consisting of about 24 $\times 10^6$ cells was adopted to simulate the overall system of the two contra-rotating propellers. Zhang et al.[29] found that the performance of the front propeller was hardly affected by the rear propeller, while that of the latter was reduced by the ingestion of the wake from the front propeller. In addition, the interaction between tip vortices was found the trigger of their faster instability. Therefore, the closer the diameters of the two propellers, the faster the instability of their wake structures. The lateral loads were reduced by the operation of the two propellers together, compared to them working in isolation.

Large eddy simulation (LES) on a grid consisting of about 15×10^6 cells was reported by Hu et al.[30] The wake topology reproduced by these computations is in good agreement with that found in the experiments by Capone and co-workers,[24–26] thanks to the accuracy of the eddy-resolving methodology. Unfortunately, despite the use of LES, no details were reported on the impact of the mutual inductance between the tip vortices of the front and rear propellers on the statistics of turbulence.

DES was also exploited by Hu et al.[31] to reconstruct the acoustic emission from contra-rotating propellers, by coupling this methodology with the Ffowcs-Williams and Hawkings acoustic analogy on a computational mesh consisting of about 7×10^6 cells. However, this study was mainly focused on the prediction of the noise originating from cavitation phenomena over the blades of the propellers, while no details were reported on the wake features and, in particular, on the dynamics of their tip vortices.

The above survey shows that little information is available in the literature on contra-rotating propellers. In addition, most studies focus on their performance, while analyses dealing with the wake features and, in particular, with their interacting tip vortices are very limited. The tip vortices play an important role in affecting downstream bodies, as rudders,[32–40] as well as in defining the acoustic signature of the system.[41–47] It is worth mentioning that a number of theoretical studies were reported in the literature on the interaction and instability of helical vortices.[48–55] The recent work by Abraham et al.[56] also analyzes the case of the helical tip vortices generated by an asymmetric rotor, where the asymmetry is aimed at accelerating the instability of the tip vortices, by promoting a faster interaction between them. A simplified model is developed for the exploration of a number of sources of asymmetry, as the extension or deflection of the rotor blades and their pitch angle. Unfortunately, all these simplified, theoretical models are targeted at providing guidance in the analysis of the interaction of the multiple vortices shed by the blades of typical rotors of propellers, helicopters or turbines, while they were not specifically designed to fit the more challenging case of the tip vortices shed by contra-rotating propellers, having opposite pitch angles and intersecting each other.

In this study, high-fidelity LES computations on a grid consisting of about 4.6×10^9 points are utilized to analyze the interaction between the tip vortices shed by contra-rotating marine propellers. As demonstrated by the literature review reported above, the adopted grid is at least two orders of magnitude more extensive than the most advanced numerical works on the subject. The impact of the shear between the tip vortices on the stability of the wake system and the statistics of turbulence is studied, relying also on direct comparisons with experimental results[24–26] on the same system as well as on LES simulations of the two propellers working alone.

In the following, this paper discusses the methodology (Sec. II), the flow problem (Sec. III), the numerical setup of the simulations (Sec. IV), the analysis of the results (Sec. V), and the final conclusions of this study (Sec. VI).

II. METHODOLOGY

The flow problem was resolved by means of the filtered Navier–Stokes equations (NSEs) for incompressible flows in non-dimensional form as follows:

$$\frac{\partial \widetilde{u}_i}{\partial x_i} = 0, \tag{1}$$

$$\frac{\partial \widetilde{u}_i}{\partial t} + \frac{\partial \widetilde{u}_i \widetilde{u}_j}{\partial x_j} = -\frac{\partial \widetilde{p}}{\partial x_i} - \frac{\partial \tau_{ij}}{\partial x_j} + \frac{1}{Re}\frac{\partial^2 \widetilde{u}_i}{\partial x_j^2} + f_i, \tag{2}$$

where the indexes $i, j = 1, 2, 3$ span the three directions in space. The quantities x_i and x_j are the coordinates in the directions i and j, respectively, t is time, $\widetilde{u}_i$ and $\widetilde{u}_j$ are the components of the filtered velocity in the directions i and j, $\widetilde{p}$ is the filtered pressure, τ_{ij} is the ij element of the subgrid scales (SGS) stress tensor, Re is the Reynolds number, and f_i is the component in the direction i of a forcing term, which is utilized to take into account the action of the bodies on the fluid in the framework of an immersed-boundary (IB) methodology.

The Reynolds number comes from scaling the NSEs by using a reference length scale, L, a reference velocity scale, U, and the density of the fluid, ρ. It is defined as $Re = LU/\nu$, where ν is the kinematic viscosity of the fluid. In this study, the diameter D of the front propeller presented in Sec. III and the free-stream velocity U_∞ are taken as reference length and velocity scales, respectively.

The SGS stress tensor comes from filtering the NSEs, that is by resolving them on a computational grid which is coarser than the Kolmogorov scale, which is the smallest scale of the flow. In particular, it originates from filtering the convective terms: $\tau_{ij} = \widetilde{u_i u_j} - \widetilde{u}_i \widetilde{u}_j$. Therefore, τ_{ij} represents the action of the unresolved scales of the flow, which cannot be resolved on the adopted computational grid, on the resolved scales. This quantity needs to be modeled. In this work, this task is performed by the wall-adaptive local eddy (WALE) viscosity model.[57] This is an eddy-viscosity model, assuming that

$$\tau_{ij}^d = -2\nu_t \widetilde{S}_{ij}, \tag{3}$$

where τ_{ij}^d is the deviatoric part of τ_{ij}, ν_t is a scalar, the eddy-viscosity, while $\widetilde{S}_{ij}$ is the deformation tensor of the resolved velocity field,

08 May 2024 09:22:52

$$\widetilde{S}_{ij} = \frac{1}{2}\left(\frac{\partial \widetilde{u}_i}{\partial x_j} + \frac{\partial \widetilde{u}_j}{\partial x_i}\right). \tag{4}$$

This way the problem of turbulence closure is reduced to modeling the only scalar eddy-viscosity. In the framework of the WALE model, this is achieved through the deviatoric part of the square of the velocity gradient tensor of the resolved field, $\mathscr{G}_{ij}$,

$$\nu_t = (C_W \Delta)^2 \frac{\left(\widetilde{\mathscr{G}}_{ij}^d \widetilde{\mathscr{G}}_{ij}^d\right)^{3/2}}{\left(\widetilde{S}_{ij}\widetilde{S}_{ij}\right)^{5/2} + \left(\widetilde{\mathscr{G}}_{ij}^d \widetilde{\mathscr{G}}_{ij}^d\right)^{5/4}}. \tag{5}$$

In Eq. (5), C_W is a constant scalar, set to 0.5, while Δ is the local resolution of the computational grid, taken as the cubic root of the volume of its cells. The expression for the eddy-viscosity in Eq. (5) allows reproducing the correct limiting behavior near solid walls, without the need of *ad hoc* corrections, which are problematic in the case of complex geometries. In addition, the WALE model automatically switches off in regions of laminar flows, where no turbulence results in $\nu_t = 0$. This SGS model was successfully validated in several studies involving marine propellers, using the same solver as in the present work.[15,58,59]

The forcing term in Eq. (2), f_i, is utilized to enforce the no-slip boundary conditions on the surface of solid bodies. In the framework of IB techniques, immersed boundaries are represented by Lagrangian grids, discretizing their surface. These grids are "immersed" within a stationary, regular Eulerian grid, discretizing the computational domain and where the NSEs are resolved. In this study, this grid is cylindrical. Based on the position of the Lagrangian grids, which are in general free to move, the Eulerian points are tagged as "solid," "fluid," and "interface." The interface points are those Eulerian points, which are placed outside the immersed boundary, but having at least a neighboring solid point. The NSEs are resolved at the fluid points of the Eulerian grid. In contrast, at the solid points, the boundary condition is the velocity of the immersed boundary. At the interface points, the boundary condition comes instead from a linear reconstruction of the solution in the direction normal to the neighboring immersed boundary. This local reconstruction is based on the no-slip requirement on the surface of the body and the solution of the flow at the closest fluid points. Therefore, at the solid and interface points, the forcing term f_i is computed as

$$f_i = \frac{V_i - \widetilde{u}_i}{\Delta t} - RHS_i, \tag{6}$$

where V_i is the boundary condition at the solid or interface point, defined as discussed above, Δt is the step of the advancement of the solution in time, and RHS_i is the sum of the viscous, convective and SGS terms of Eq. (2), which are discretized explicitly. Also, the IB technique adopted in this work was successfully utilized in a number of our earlier studies dealing with marine propellers.[15,58,59] More details on its implementation and validations on canonical flow problems can be found in the works by Balaras and co-workers.[60,61]

Equations (1) and (2) were resolved on a staggered, cylindrical grid. Second-order, central finite-differences were adopted to discretize their derivatives in space. The advancement of the solution in time was based on a fractional-step approach.[62] The explicit, three-step Runge–Kutta scheme was utilized for the discretization in time of the radial and axial derivatives. The implicit, Crank–Nicolson scheme was

instead adopted for the discretization in time of the azimuthal derivatives: the anisotropy of the cylindrical grid at the axis required the use of an implicit approach to relax the otherwise prohibitive stability requirements. The hepta-diagonal Poisson problem arising from the discretization of Eq. (1) was resolved by using trigonometric transformations along the azimuthal direction, resulting into a penta-diagonal problem for each meridian slice of the cylindrical grid. Each of them was inverted by using a direct Poisson solver,[63] rather than costly iterative techniques, to benefit the efficiency of the overall solver.

III. FLOW PROBLEM

LES computations were carried out on a system of contra-rotating propellers, consisting of a three-bladed front propeller and a three-bladed rear propeller, rotating with the same angular speed, Ω, but in opposite directions. Its geometry is shown in Fig. 1, including upstream and downstream shafts. The two upstream and downstream shafts are stationary, the front propeller rotates with a positive angular speed, while the rear propeller with a negative angular speed. The system was simulated in open-water conditions, with the front propeller ingesting a uniform flow. In the following, this case will be indicated as *CRP*. All dimensions were scaled by the diameter of the front propeller, D. The rear propeller is characterized by a smaller diameter, $d = 0.91D$. The origin of the reference frame was placed on the axis of the system between the two propellers, at the interface between their hubs. Also the isolated front and rear propellers were simulated by replacing each of them using a dummy hub, that is a cylinder rotating at the same angular speed as the propeller it is replacing. This is the same strategy adopted in the experiments[24–26] we utilized as a reference for validation purposes. The cases of the propellers working alone will be denoted below as *FRONT* and *REAR*, respectively. Their geometries are represented in the panels (a) and (b) of Fig. 2.
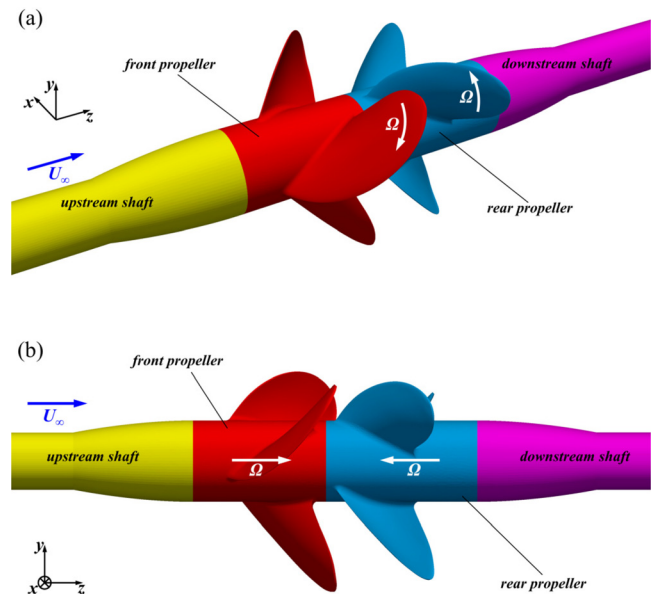

FIG. 1. Geometry of the *CRP* configuration with the two contra-rotating propellers working together: (a) isometric view and (b) lateral view.
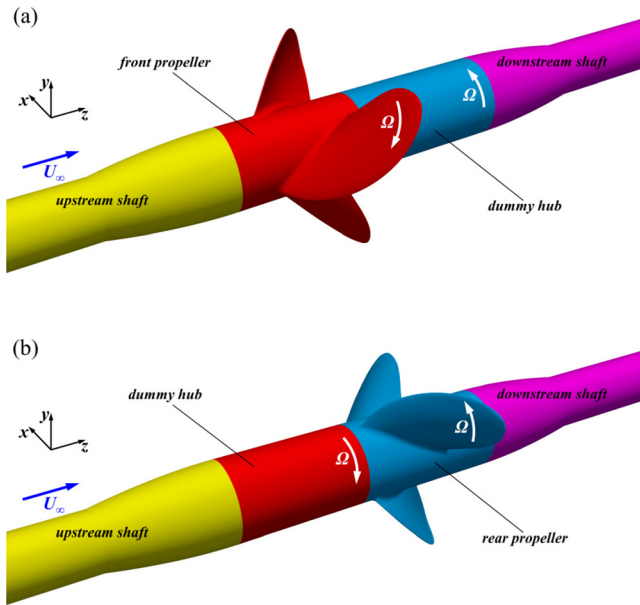
FIG. 2. Geometry of the (a) *FRONT* and (b) *REAR* configurations with the front and rear propellers working alone.

The working conditions of marine propellers are typically characterized by the advance coefficient, J, and the Reynolds number, Re_p. The advance coefficient is defined as

$$J = V/nD, \qquad (7)$$

where V is the advance velocity, in this case equal to the free-stream velocity, U_∞, while n is the frequency of the rotation of the propeller. In the present study, a value $J = 0.7$ was simulated. This is equivalent to a load condition significantly higher than design ($J \approx 1.4$), generating stronger wake structures, as the tip vortices, which are the main subject of this work. The Reynolds number is defined as

$$Re_p = \frac{c_{0.7R} W_{0.7R}}{\nu}, \qquad (8)$$

where $c_{0.7R}$ is the chord of the blades of the front propeller at 70% of its radial extent, R, and $W_{0.7R} = \sqrt{V^2 + (0.7 \times 2\pi n \times R)^2}$ is the magnitude of the relative velocity of the flow at the same radial location. In the present simulations, the Reynolds number was equal to about 250 000.

The results of the computations are compared against experimental measurements[24–26] on the parameters of performance of the system of the two propellers as well as on the same propellers working alone. In the framework of the same experimental study, high-resolved visualizations of the dynamics of the tip vortices shed by the contra-rotating propellers were also captured. They will be compared with the results of the present simulations to verify the complex topology of the wake structures. The experiments were conducted on front and rear propellers with diameters $D = 218.71$ mm and $d = 198.94$ mm, respectively. Their chords at 70% of their radial extent were equal to 81.90 and 74.52 mm. The diameter of the hub was equal to 68.23 mm.

An advance velocity $V = 3.68$ m/s and a rotational frequency $n = 24$ Hz were considered for the experiments at the advance coefficient $J = 0.7$.

IV. COMPUTATIONAL SETUP

All LES computations were carried out within a cylindrical domain, illustrated in Fig. 3, having a radial extent equal to 5.0D. The inflow and outflow boundaries were placed respectively 3.0D upstream and 5.0D downstream of the origin of the streamwise coordinates, which was placed between the two propellers. To reproduce the same conditions as in the experiments,[24–26] a uniform streamwise velocity U_∞ was enforced at the inlet boundary of the domain, while convective conditions were utilized on all three velocity components at the outlet boundary, using U_∞ as convective velocity. Slip-wall conditions for velocity were imposed at the cylindrical boundary of the domain, to mimic a free-stream. Homogeneous Neumann conditions were enforced for both pressure and eddy viscosity at all boundaries of the computational domain. The no-slip requirement on the surface of
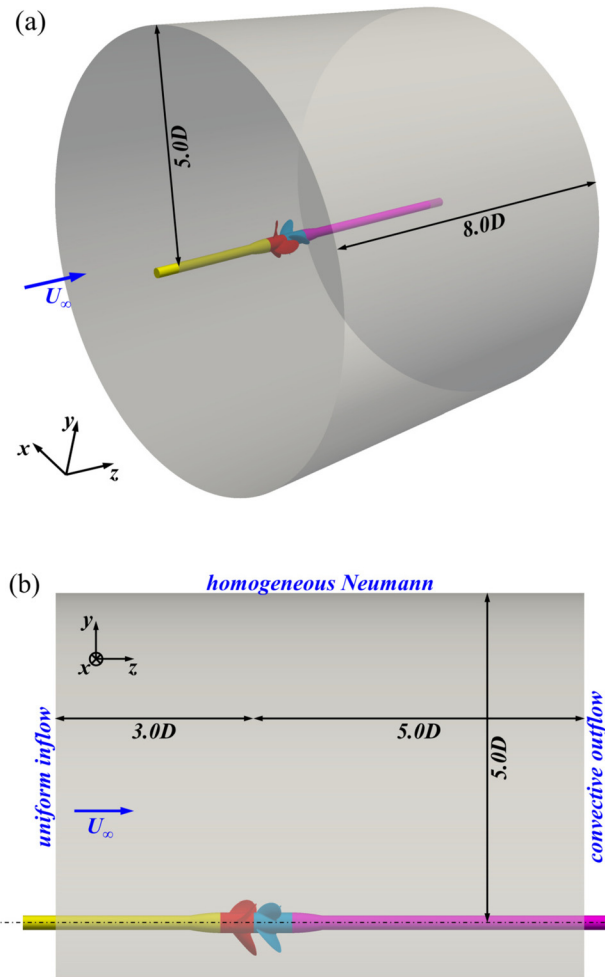

FIG. 3. Cylindrical domain of the computations: (a) isometric view and (b) lateral view.

08 May 2024 09:22:52

both shafts and propellers was imposed by means of an IB methodology, as discussed in Sec. II.

The IB technique discussed in Sec. II allowed us using a single-block, stationary cylindrical grid to discretize the whole computational domain. It was composed of $722 \times 3586 \times 1794$ (about 4.6×10^9) points in the radial, azimuthal, and axial directions, respectively. This grid was characterized by a uniform angular spacing in the azimuthal direction, while stretching was adopted in the radial and axial directions to cluster points in the regions of the propellers and their wake. Details on the distribution of the grid spacing are reported in Fig. 4. Visualizations of the grid in the vicinity of the propellers are also reported in Fig. 5. It is worth noting that for visibility of the grid lines only a sample of points is shown in Fig. 5. As discussed above, the Eulerian grid is not body-fitted and the representation of the geometry of the bodies relies on the Lagrangian grids immersed within the Eulerian grid. Figure 4(a) shows that the radial spacing of the grid is uniform, $\Delta r = 7.5 \times 10^{-4}D$, up to almost $r/D = 0.6$, in order to resolve properly the blades of the propellers as well as their tip vortices. The choice of extending the region of the finest radial resolution beyond the tip of the blades is explained by the following discussion of the results, which demonstrate that the wake of the *CRP* system experiences even an expansion, due to the interaction between the tip vortices shed by the two propellers. Figure 4(b) shows the distribution of the grid spacing in the streamwise direction. This is uniform in the region of the two propellers $-0.35 < z/D < 0.45$, where $\Delta z = 7.5 \times 10^{-4}D$, as in the radial direction. Further downstream grid stretching is adopted, but keeping a fine resolution of the mesh, with the purpose of resolving the wake structures. It should be also noted that, although a uniform azimuthal grid was utilized, thanks to
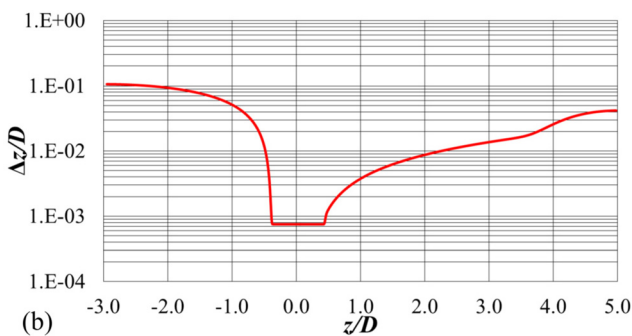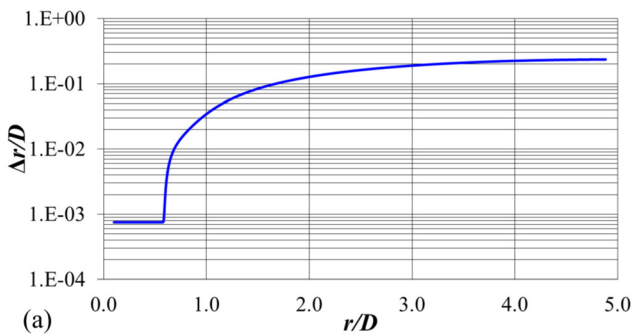

FIG. 4. (a) Radial and (b) axial distributions of the grid spacing.
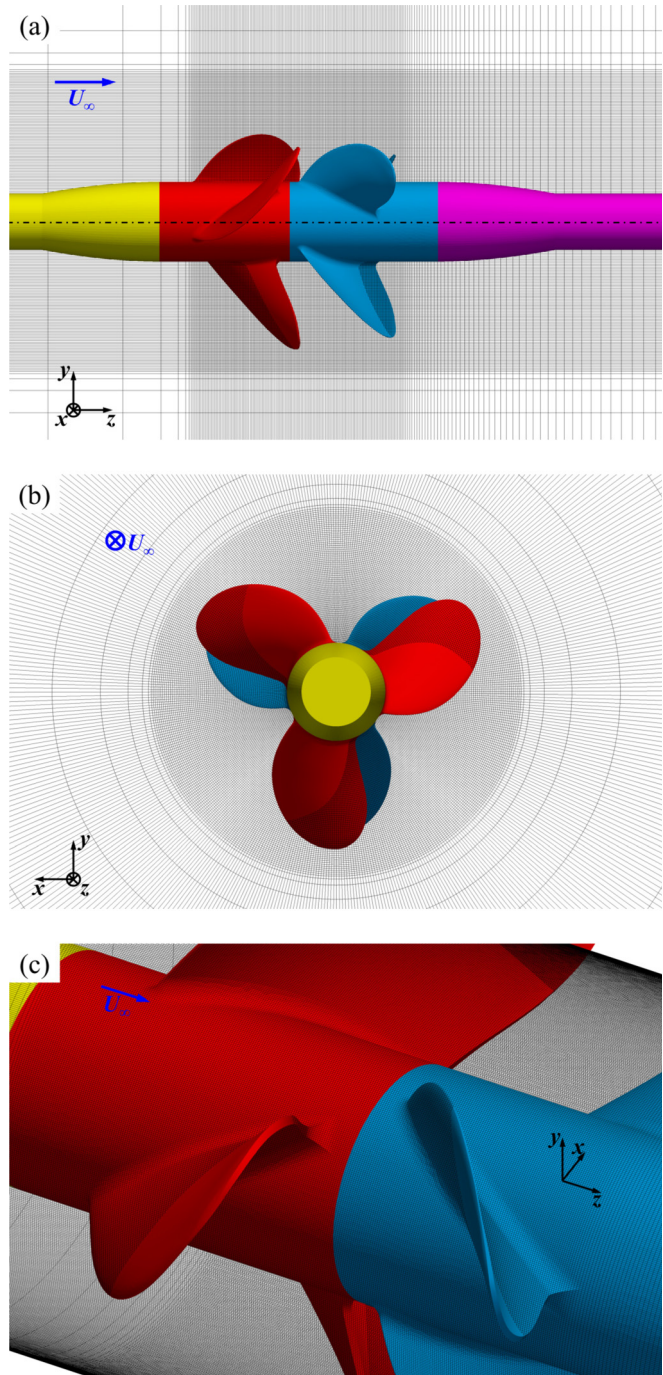

FIG. 5. Details of the cylindrical, fine grid in the vicinity of the propellers: (a) meridian, (b) cross-stream, and (c) cylindrical slices. For clarity, 1 of every 64 points shown in panels (a) and (b) and 1 of every 16 points in panel (c).

the cylindrical topology of the mesh, the linear spacing in the azimuthal direction is actually decreasing toward inner radial coordinates, which is convenient to properly resolve the flow physics in the region of interest of the domain, where the propellers and their wakes are

located. For instance, at the radial coordinate corresponding to 70%R, the linear resolution of the computational grid in the azimuthal direction is $0.7R\Delta\vartheta = 6.1 \times 10^{-4}D$, similar to those in the radial and axial directions. Overall, we verified a near-wall resolution of the adopted mesh equivalent to about five wall-units.

The one discussed above is the computational (fine) grid adopted for the simulation of the three *CRP*, *FRONT*, and *REAR* configurations. However, with the purpose of demonstrating grid-independence, the *CRP* case was simulated also on two additional grids, denoted as medium and coarse. They consist of $572 \times 2818 \times 1410$ (about 2.3×10^9) and $454 \times 2370 \times 1186$ (about 1.3×10^9) points. They were generated by increasing the size of the grid cells in each direction in space of factors equal to about $2^{1/3}$ and $2^{2/3}$ for the medium and coarse grids, respectively, relative to the fine grid. The discussion in Sec. V will show a robust grid independence, demonstrating that the results on the fine grid are at convergence. Note that, unless otherwise stated, all results in Sec. V refer to the computations carried out on the fine grid.

As discussed in Sec. II, the geometry of the system was represented by using Lagrangian grids, discretizing the surface of the bodies by triangular elements. Thanks to the exploitation of an IB methodology, they were immersed within the stationary Eulerian grid and free to move across its cells, to take into account the rotation of the propellers. This feature of the IB method avoids the use of multi-block grids with interfaces between them or other strategies, as mesh deformation techniques or multiple reference frames. This approach produces a substantial simplification of the process of generation of the Eulerian grid and is beneficial to both the accuracy and the efficiency of the overall formulation. The *CRP* system utilized Lagrangian grids consisting of 66 132 (front propeller), 69 048 (rear propeller), 32 286 (upstream shaft), and 51 048 (downstream shaft) triangles. These surface meshes are represented in Fig. 6. In the case *FRONT*, the rear propeller was replaced by a rotating cylinder, represented by 10 308 triangles, while for the case *REAR*, the front propeller was replaced by a rotating cylinder consisting of 9648 triangles. They are shown in Fig. 7.

The resolution in time was tied to that in space through the stability requirements of the Runge–Kutta scheme adopted for the explicit discretization of the radial and axial terms of the momentum equation. In the case *CRP*, this resulted in an average time step of the simulations corresponding to rotations of $0.052°$, $0.068°$, and $0.070°$ of both front and rear propellers on the fine, medium, and coarse grids, respectively. In the cases *FRONT* and *REAR*, the average time step resulted in a rotation of $0.050°$ and $0.049°$ of the front and rear propellers, respectively, on the fine grid. These values show how the reported computations are highly time-resolved.

All computations were advanced in time for at least two flow-through times, equivalent to about 20 rotations, to develop the wake flow and reach statistically steady conditions. Then, both ensemble-averaged and phase-averaged statistics were computed on the fly during the simulations, across 20 additional revolutions of the propellers. Ensemble-averaged statistics are time-averages, computed from all instantaneous realizations of the solution, regardless of the relative position between propellers. They will be indicated in Sec. V as $\overline{\cdot}$. Phase-averaged statistics are instead computed considering only instantaneoues realizations of the solution corresponding to a specific relative, angular position of the contra-rotating propellers. They will be denoted below as $\hat{\cdot}$.

In the following discussion, the velocity components across the radial, azimuthal, and streamwise directions will be indicated as u, v,
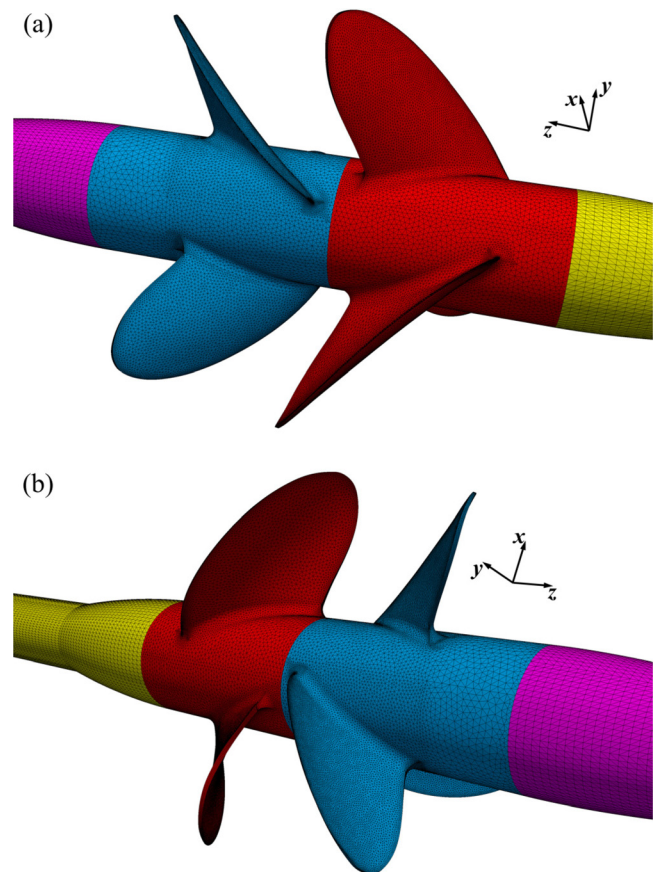

FIG. 6. Lagrangian grids of the *CRP* system. Views on the (a) suction and (b) pressure sides of the propeller blades.

and w, respectively. Their fluctuations in time will be reported as u', v', and w'. Therefore, the ensemble averaged and phase-averaged turbulent kinetic energy discussed below are defined, respectively, as

$$\overline{k} = \frac{1}{2}\left(\overline{u'}^2 + \overline{v'}^2 + \overline{w'}^2\right), \tag{9}$$

$$\hat{k} = \frac{1}{2}\left(\hat{u'}^2 + \hat{v'}^2 + \hat{w'}^2\right). \tag{10}$$

Also the ensemble-averaged turbulent shear stresses will be analyzed. They will be indicated as $\overline{u'w'}$, $\overline{u'v'}$, and $\overline{v'w'}$. It is also worth mentioning that all discussions will refer to resolved quantities. Therefore, for convenience, the notation $\overline{\cdot}$ for the filter operator, adopted in Sec. II, will be omitted.

All simulations were carried out in a high performance computing environment. An in-house Fortran solver was adopted to resolve the filtered NSEs, performing a domain decomposition across the streamwise direction. Therefore, the overall problem was decomposed in cylindrical subdomains and spread across cores of a distributed-memory supercomputer (MeluXina CPU at LuxProvide, Luxemburg). In particular, the computations on the fine, medium, and coarse grids were distributed across 1792, 1408, and 1184 cores. Communications between subdomains were handled by means of calls to message
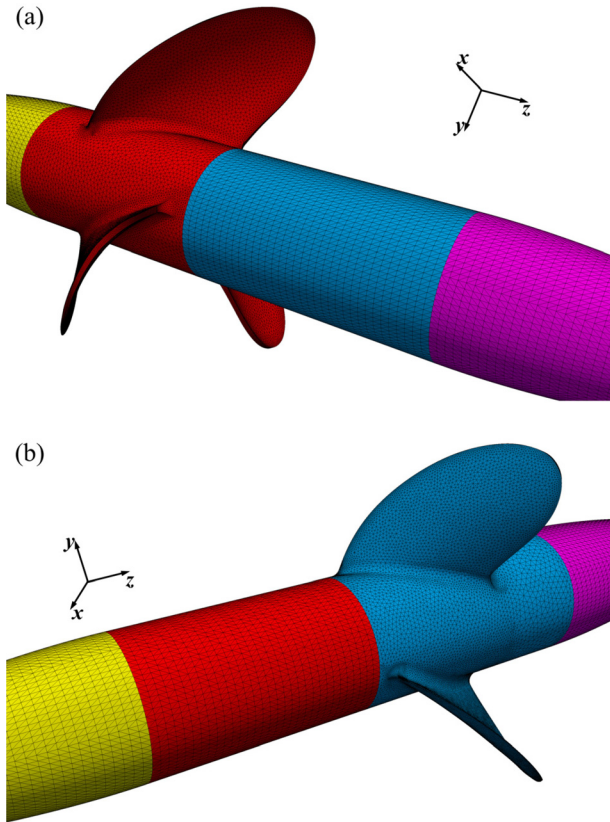
FIG. 7. Lagrangian grids of the (a) *FRONT* and (b) *REAR* systems.

TABLE I. Comparison on the global parameters of performance against the experiments[24–26] for the front propeller working alone.

	$\overline{K}_T$	$10\overline{K}_Q$	$\overline{\eta}$
Experiments[24–26]	0.384	0.898	47.7%
LES/IB computation	0.388	0.883	48.9%
Relative error	+0.95%	−1.59%	+2.58%

TABLE II. Comparison on the global parameters of performance against the experiments[24–26] for the rear propeller working alone.

	$\overline{K}_T$	$10\overline{K}_Q$	$\overline{\eta}$
Experiments[24–26]	0.303	0.762	44.3%
LES/IB computation	0.308	0.743	46.2%
Relative error	+1.79%	−2.54%	+4.44%

TABLE III. Comparison on the global parameters of performance against the experiments[24–26] for the front propeller of the *CRP* configuration.

	$\overline{K}_T$	$10\overline{K}_Q$	$\overline{\eta}$
Experiments[24–26]	0.382	0.871	48.9%
Coarse LES/IB computation	0.389	0.874	49.6%
Relative error	+1.76%	+0.30%	+1.46%
Medium LES/IB computation	0.390	0.871	50.0%
Relative error	+2.13%	−0.05%	+2.18%
Fine LES/IB computation	0.392	0.869	50.2%
Relative error	+2.44%	−0.23%	+2.68%

TABLE IV. Comparison on the global parameters of performance against the experiments[24–26] for the rear propeller of the *CRP* configuration.

	$\overline{K}_T$	$10\overline{K}_Q$	$\overline{\eta}$
Experiments[24–26]	0.350	0.876	44.5%
Coarse LES/IB computation	0.351	0.882	44.3%
Relative error	+0.37%	+0.63%	−0.26%
Medium LES/IB computation	0.355	0.882	44.8%
Relative error	+1.43%	+0.68%	+0.74%
Fine LES/IB computation	0.357	0.886	44.8%
Relative error	+1.99%	+1.15%	+0.83%

passing interface (MPI) libraries. The overall computational cost of all simulations was of about 13×10^6 core hours.

V. RESULTS

A. Global performance

Results on the parameters of global performance of the propellers are reported in this section, to demonstrate the agreement with the relevant measurements.[24–26] They are defined as follows:

$$K_T = \frac{T}{\rho n^2 D^4}, \quad K_Q = \frac{Q}{\rho n^2 D^5}, \quad \eta = \frac{J K_T}{2\pi K_Q}. \quad (11)$$

In Eq. (11), T and Q are the thrust generated by the propeller and the torque required for its rotation, respectively. The coefficients of thrust and torque, K_T and K_Q, are their expressions in non-dimensional form. The non-dimensional quantity η represents the efficiency of propulsion.

Tables I and II report the comparison of the parameters of performance of the isolated front and rear propellers against the experiments.[24–26] A close agreement between LES and experiments is shown. As discussed above, for the two propellers working together, computations were conducted on three grid levels. Comparisons are reported in Tables III and IV for the front and rear propellers, respectively. For both propellers, a good agreement with the experiments is verified even on the coarse grid.

The comparison of the global performance of the propellers working alone and together shows a slight improvement for the front propeller, whose efficiency of propulsion goes from 48.9% to 50.2%, based on the LES computations on the fine grid. This trend is also observed in the experimental results. This should be attributed to the blockage generated by the rear propeller, affecting the distribution of
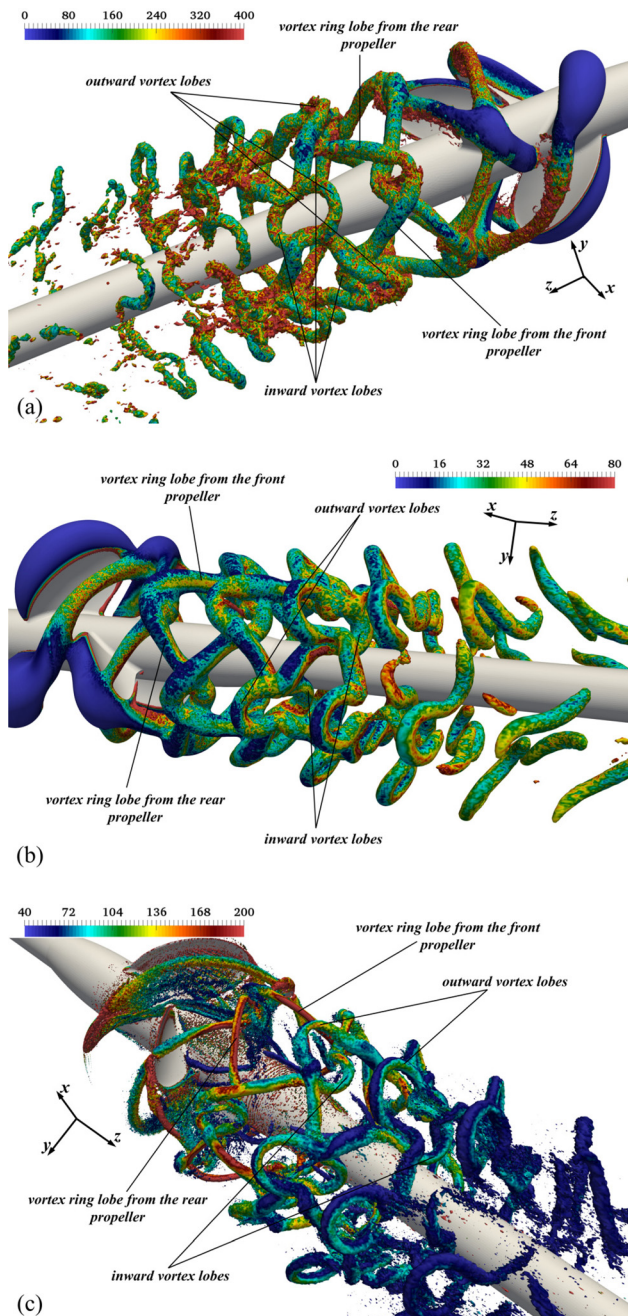
FIG. 8. (a) Instantaneous isosurfaces of pressure coefficient ($c_p = -1.0$); (b) phase-averaged isosurfaces of pressure coefficient ($\hat{c}_p = -0.5$); and (c) phase-averaged isosurfaces of the second invariant of the velocity gradient tensor (Q-criterion, $QD^2/U_\infty^2 = 500$). Contours of vorticity magnitude, scaled by U_∞/D. Visualizations from the data on the fine grid.

FIG. 9. Instantaneous isosurfaces of pressure coefficient ($c_p = -2.0$) highlighting (a) the intersection of the tip vortices shed by the front and rear propellers, (b) their merging in isolated vortex rings, (c) the onset of U-shaped vortex lobes connecting the helical sides of the vortex rings, and (d) the projection of the U-shaped vortex lobes toward inner and outer radial coordinates. Contours of vorticity magnitude, scaled by U_∞/D. Visualizations from the data on the fine grid. Multimedia available online.

the pressure field, especially on the pressure side of the blades of the front propeller. In contrast, a slight decay of the performance occurs for the rear propeller: $\overline{\eta}$ goes from 46.2% to 44.8%, based on the results on the fine grid, but it should be acknowledged that the

efficiency of the rear propeller is almost unchanged in the experimental results.

B. Wake topology

The interaction between the helical vortices shed by the two propellers results in the generation of isolated vortex rings, consisting of six helical sides and connected by U-shaped vortex lobes. This complex structure is illustrated in Fig. 8. The wake coherence is isolated in Fig. 8 through both isosurfaces of pressure coefficient and the Q-criterion. The former is defined as $c_p = (p - p_\infty)/(0.5\rho U_\infty^2)$, where p_∞ is the free-stream pressure. The latter is the second invariant of the velocity gradient tensor, which is appropriate to identify the core of vortices, as discussed by Jeong and Hussain.[64]

At their closest point of interaction, represented in Fig. 9(a), near the blade tips of the rear propeller, the two vortex systems from the front and rear propellers break up and immediately reconnect by cross-pairing between them, leading to the formation of a single closed vortex ring, as shown in Fig. 9(b). The helical lobes of the vortex rings, originating alternatively from the tip vortices of the front and rear propellers, are linked through U-shaped vortex lobes [Fig. 9(c)]. They experience a shift toward inner and outer radial coordinates, as a result of the mutual inductance between consecutive vortex rings [Fig. 9(d)] (Multimedia available online). This unique topology was first identified experimentally by Capone and Alves Pereira[24] and is here revealed in

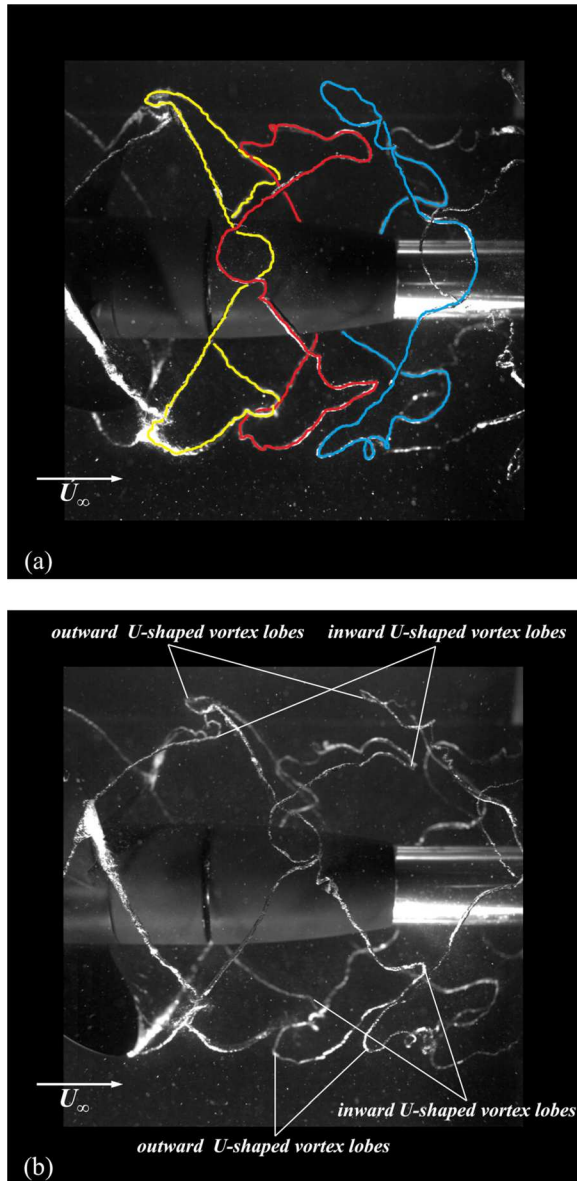
FIG. 10. Visualizations of the tip vortices in the near wake from experiments:[24–26] (a) identification of three consecutive vortex rings and (b) identification of the U-shaped vortex lobes connecting the six sides of each vortex ring.
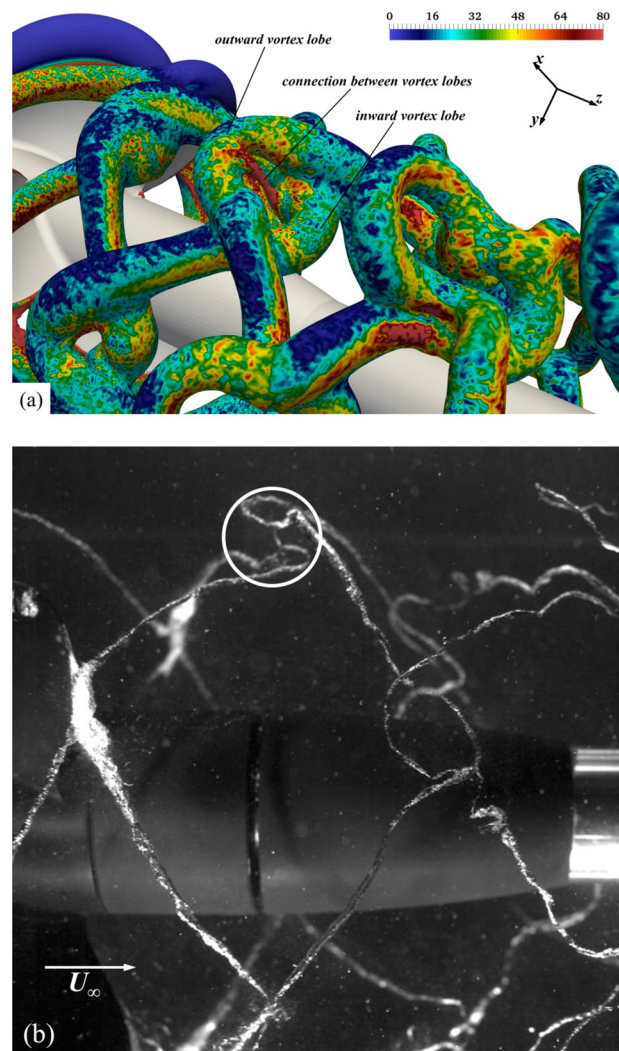

FIG. 11. (a) Phase-averaged isosurfaces of pressure coefficient ($\hat{c}_p = -0.5$) from LES (fine grid), with contours of vorticity magnitude, scaled by U_∞/D and (b) visualization of the vortex filament connecting neighboring vortex lobes from experiments.[24–26]

more details by the simulations, which are in excellent agreement with the experiments performed on the same contra-rotating configuration, illustrated in Fig. 10. Each ring consists of three helical lobes originating from the front propeller and three helical lobes from the rear propeller. The helical lobes of each vortex ring are connected by three upstream and three downstream U-shaped lobes, bending outwards and inwards, as a consequence of their interaction with the upstream

(a)

(b)

(c)

FIG. 12. Phase-averaged isosurfaces of the second invariant of the velocity gradient tensor (Q-criterion, $\hat{Q}D^2/U_\infty^2 = 1,000$): (a) fine, (b) medium, and (c) coarse grids. Contours of vorticity magnitude, scaled by U_∞/D.

and downstream vortex rings, respectively. Interestingly, the agreement between LES computations and experiments extends even to the identification of a short and intense vortex filament connecting neighboring inward and outward U-shaped lobes during the early stages after their onset, as they move away from each other, as shown in the details of Fig. 11 from both computations and experiments.

Figure 12 shows also that the complex topology of the wake flow revealed by the simulations is grid-independent. Results on the fine, medium, and coarse grids are reported. The agreement across grids is very satisfactory, showing almost identical vortex rings as well as outward and inward U-shaped lobes connecting their six sides. Figure 12 provides further evidence that the adopted resolution is very well suited to capture the multiple structures populating the wake of the contra-rotating propellers.

C. Wake expansion

As shown in Fig. 13(a), the outward shift of the vortex lobes of the vortex rings causes an expansion of the wake of the *CRP* system, which is in contrast with the wake contraction of conventional propellers, as demonstrated by the comparison against the wakes of the two isolated front and rear propellers in Figs. 13(b) and 13(c), respectively. The signature of this behavior on the average flow field is shown in
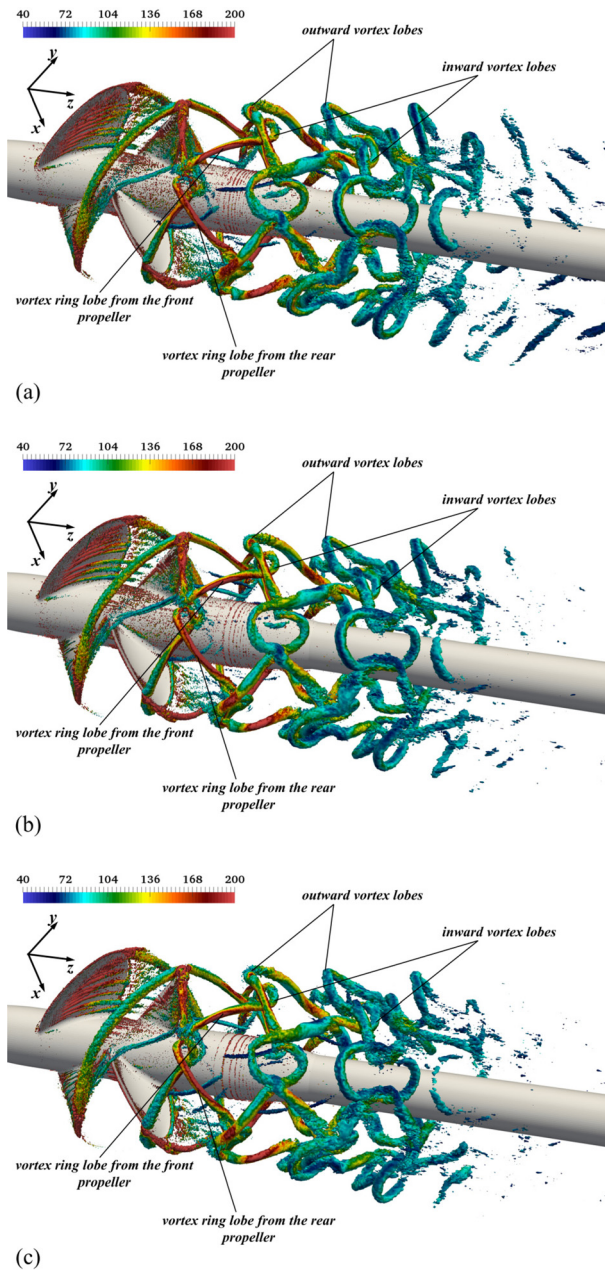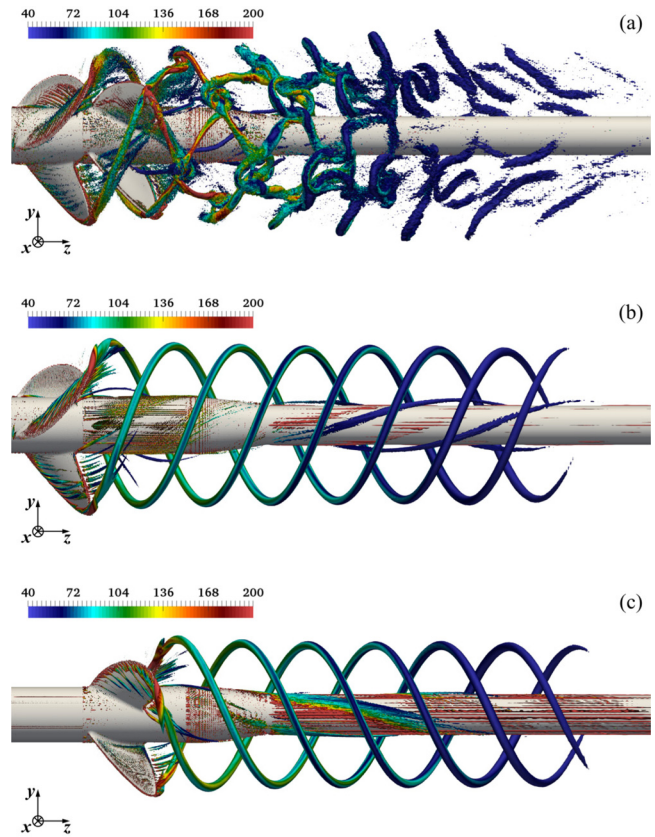

(a)

(b)

(c)

FIG. 13. Phase-averaged isosurfaces of the second invariant of the velocity gradient tensor (Q-criterion, $\hat{Q}D^2/U_\infty^2 = 500$), colored by contours of vorticity magnitude, scaled by U_∞/D: (a) *CRP*; (b) *FRONT*; and (c) *REAR*.
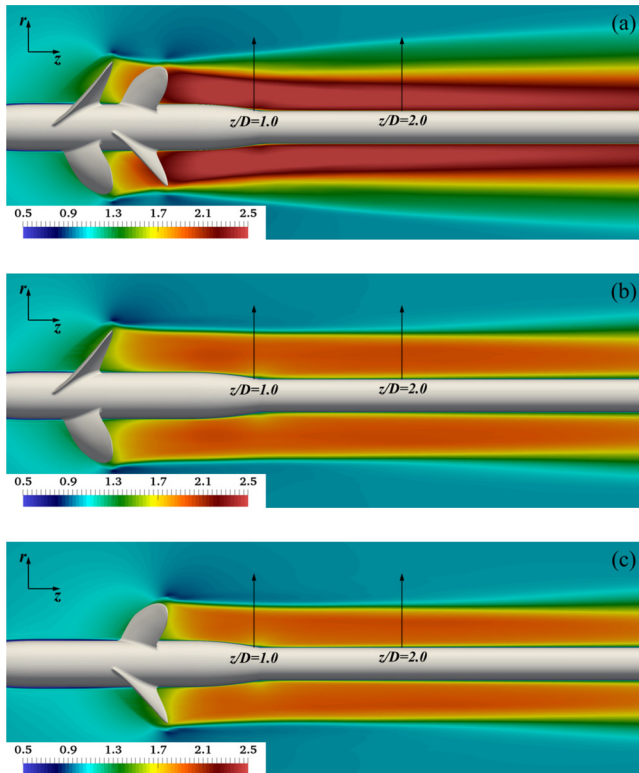
08 May 2024 09:22:52

FIG. 14. Ensemble-averaged contours of streamwise velocity, scaled by U_∞, on a meridian slice: (a) *CRP*; (b) *FRONT*; and (c) *REAR*.

FIG. 15. Radial profiles of ensemble-averaged streamwise velocity at the streamwise locations indicated by arrows in Fig. 14: (a) $z/D = 1.0$ and (b) $z/D = 2.0$.

Fig. 14, where ensemble-averaged statistics are reported for the streamwise velocity, including also the cases of the two isolated propellers. More details are provided by means of the radial profiles in Fig. 15, which were extracted from the ensemble-averaged fields of streamwise velocity at $z/D = 1.0$ and $z/D = 2.0$ (arrows in Fig. 14). While the stronger acceleration of the flow downstream of the two propellers working together is expected, Fig. 15 also shows that this acceleration extends to outer radial coordinates, in comparison with the cases of the isolated propellers. This is a consequence of the outward shift of the upstream U-shaped vortex lobes of the vortex rings populating the wake of the contra-rotating propellers.

Wake expansion as well as an increased complexity of the topology are also well distinguishable from the ensemble-averaged fields of azimuthal vorticity in Fig. 16 and the relevant radial profiles in Fig. 17. It is worth noting that in Fig. 17, the maxima of vorticity are higher in the wake of the isolated front and rear propellers than downstream of *CRP*: the instability of the wake system in the latter case is faster, resulting in two broader, more diffused, lower maxima of vorticity, in contrast with the single, sharper peak produced in the wake of both isolated propellers.

Additional evidence of the grid-independence of the results is provided in Fig. 18, where radial profiles for the ensemble-averaged streamwise velocity and azimuthal vorticity at the streamwise coordinate $z/D = 1.0$ are compared across resolutions. The agreement across grids is very close.
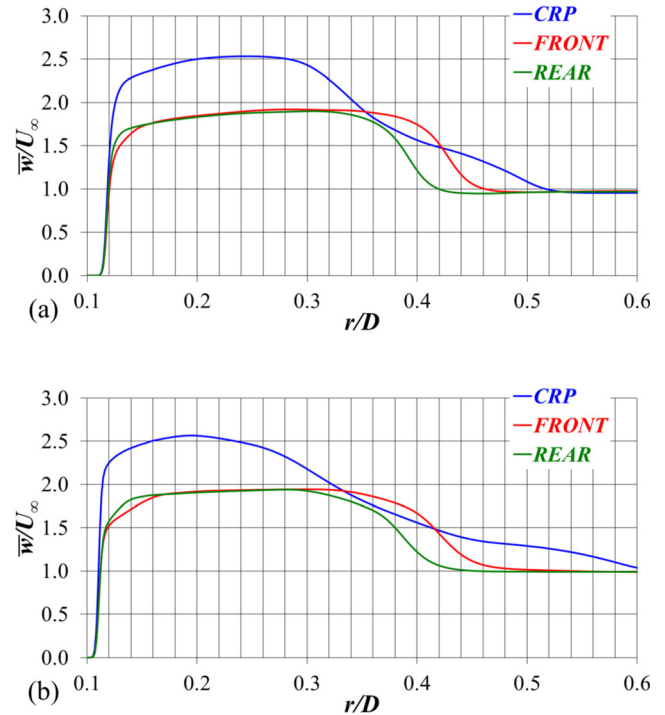
D. Phase-averaged turbulent kinetic energy

Results for turbulent kinetic energy are reported in terms of phase-averaged statistics in Fig. 19, where the meridian slice crosses the helical lobes of the vortex rings, as illustrated also by means of three-dimensional visualizations of the coherent structures shed by the two propellers. It is worth noting that the lobes originating from the tip vortices shed by the rear propeller are populated by higher levels of turbulent kinetic energy, compared to those from the front propeller, since the rear propeller ingests the turbulent wake of the front one. Therefore, the meridian slice shown in Fig. 19 is characterized by maxima of turbulent kinetic energy at the outer boundary of the wake which display a non-monotonic trend, since they originate alternatively from the front and rear propellers, whose signature is indicated as F and R, respectively. This asymmetry between levels of turbulent kinetic energy within the vortex ring lobes coming from the front and rear propellers is also demonstrated in the cross sections of Fig. 20.

Figure 21 deals again with contours of phase-averaged turbulent kinetic energy, but in this case, the meridian slice crosses the U-shaped lobes connecting the helical lobes of the vortex rings. In this visualization of the wake, the outward and inward shifts of the U-shaped vortex lobes are well distinguishable. Also, the signature C of the radial structure connecting those vortices just downstream of their onset is revealed by the relevant local maxima of turbulent kinetic energy, linking the peaks I and O at inner and outer radial coordinates, associated with the cores of the inward and outward vortex lobes of the wake system.
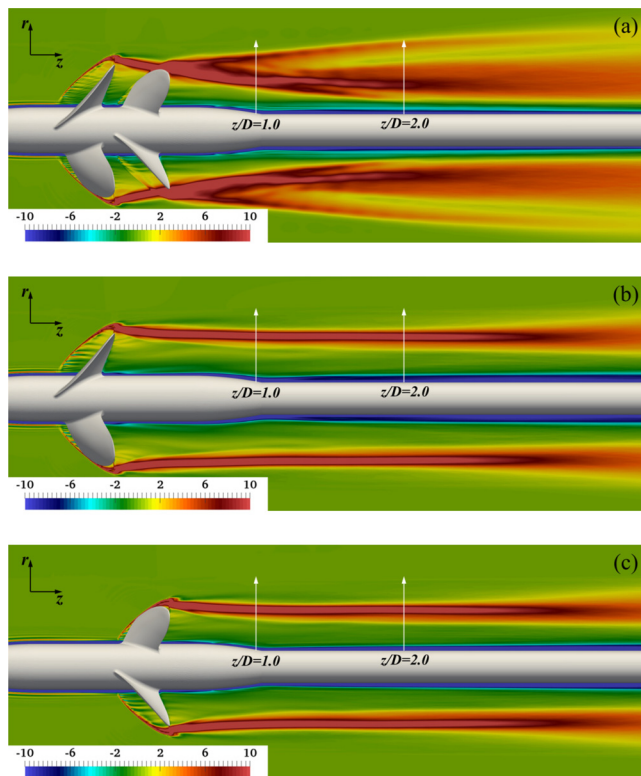
FIG. 16. Ensemble-averaged contours of azimuthal vorticity, scaled by U_∞/D, on a meridian slice: (a) *CRP*; (b) *FRONT*; and (c) *REAR*.

FIG. 17. Radial profiles of ensemble-averaged azimuthal vorticity at the streamwise locations indicated by arrows in Fig. 16: (a) $z/D = 1.0$ and (b) $z/D = 2.0$.

Additional details are provided in Fig. 22, where the areas of shear between outward and inward lobes of consecutive vortex rings are identified by arrows as those of the highest levels of turbulent kinetic energy.

E. Ensemble-averaged turbulent kinetic energy

Figure 23 represents contours of ensemble-averaged turbulent kinetic energy on a meridian slice. For more insight on the effect of the interaction between tip vortices, also the results in the wake of the isolated propellers are reported. The visualizations in Fig. 23 provide further evidence of the expansion of the propeller wake, resulting from the interaction of the helical tip vortices shed by the two propellers. In addition, the comparison with the wakes of the isolated propellers makes it clear that higher levels of turbulent kinetic energy are achieved in the near wake, as a result of this interaction. Meanwhile, the diffusion of the maxima of turbulence at the outer boundary of the wake is faster, as a consequence of the faster instability of the wake system, resulting quickly in broader maxima, compared to the wake of the two isolated propellers.

A more detailed comparison across cases, dealing with the data in Fig. 23, is available in Fig. 24, where radial profiles were extracted at the streamwise coordinates (a) $z/D = 0.5$, (b) $z/D = 1.0$ and (c) $z/D = 2.0$. Figure 24(a) shows that the interaction between tip vortices produces higher values of turbulent kinetic energy in the near wake: the peak at the outer boundary of the wake is both higher and wider, compared to the cases of the isolated propellers. This trend is
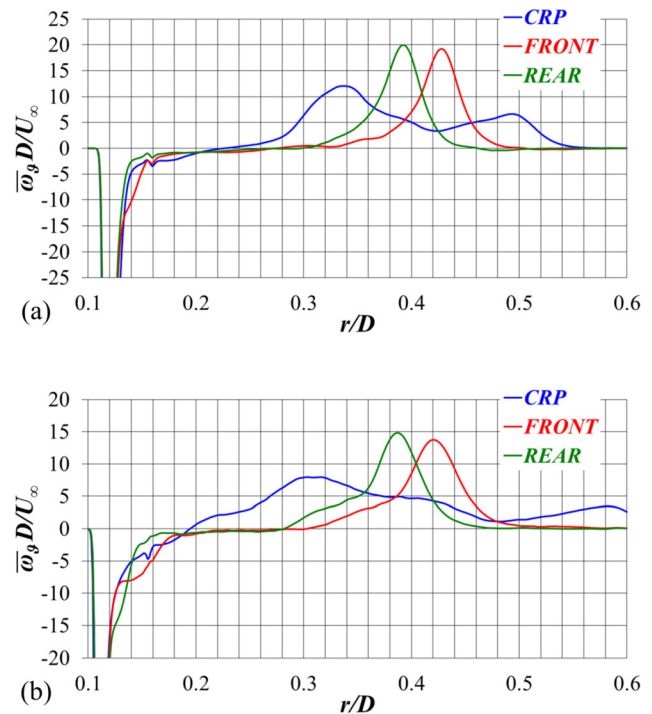
even reinforced further downstream in Fig. 24(b), where the peak of turbulent kinetic energy moves to inner radial coordinates, but its tail extends further away from the axis, which is the signature of the outward projection of the U-shaped lobes linking the six helical sides of the vortex rings. In Fig. 24(c) the peak in the wake of *CRP* weakens and becomes comparable to that of the cases *FRONT* and *REAR*, although the integral value for *CRP* keeps well above those of the isolated propellers: turbulence is higher at both inner ($0.2 < r/D < 0.3$) and outer ($0.5 < r/D < 0.6$) radial coordinates, due to the inward and outward shifts of the downstream and upstream U-shaped vortex lobes, respectively.

Grid-independence is demonstrated also for turbulent kinetic energy in Fig. 25, where radial profiles are given at the streamwise location $z/D = 1.0$ on the fine, medium and coarse grids: they almost overlap across resolutions.

Figure 26 shows the streamwise evolution of the maxima of ensemble-averaged turbulent kinetic energy at the outer boundary of the wake, corresponding to the region of the tip vortices. Just downstream of the rear propeller the *CRP* and *REAR* cases display similar maxima. Values are lower in the *FRONT* case, since its tip vortices were generated more upstream. However, the levels of turbulence become quickly the highest for *CRP*, as a consequence of the shear between the tip vortices of the two propellers and their faster instability. Interestingly, this interaction produces local maxima and minima across the streamwise evolution through the near wake, which vanish once the instability of the tip vortices causes the wake of *CRP* to lose its coherence. Eventually, the peak values for *CRP* drop to similar levels of the cases *FRONT* and *REAR* due to the diffusion of the maxima of
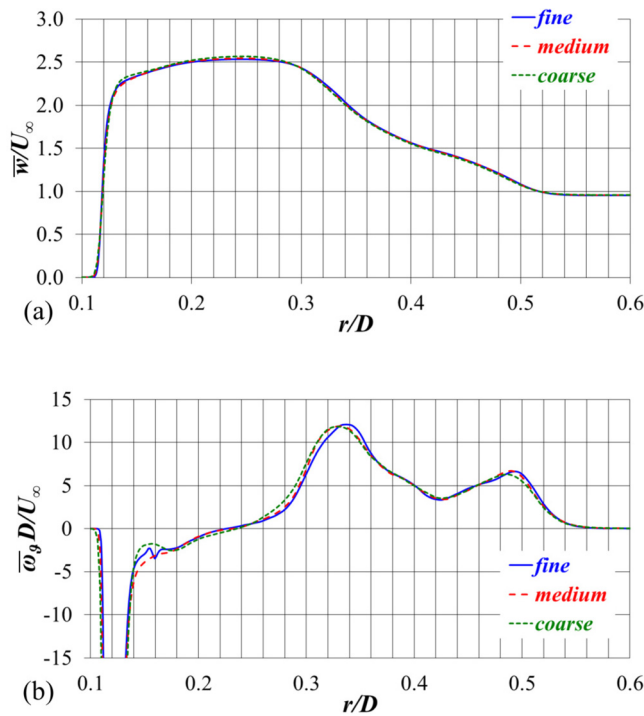
08 May 2024 09:22:52

FIG. 18. Radial profiles of ensemble-averaged (a) streamwise velocity and (b) azimuthal vorticity at the streamwise location $z/D = 1.0$ from the computations dealing with the *CRP* system on the fine, medium, and coarse grids.
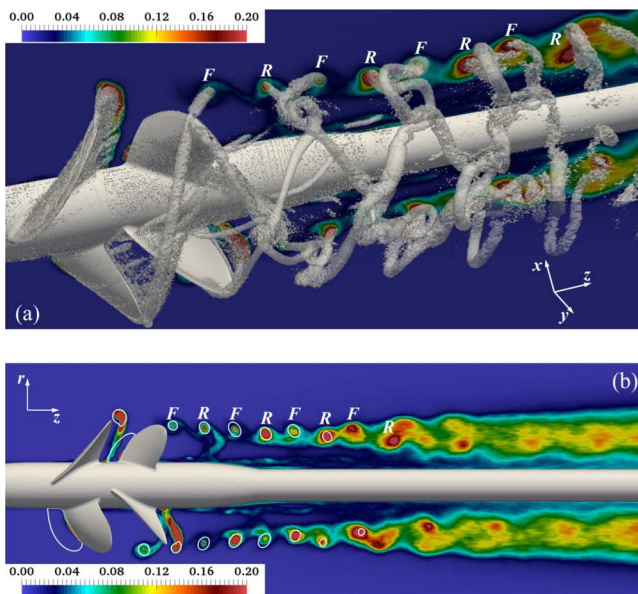

FIG. 19. Contours of phase-averaged turbulent kinetic energy, scaled by U_∞^2, in the wake of *CRP* on a meridian slice cutting the helical lobes of the vortex rings of the wake system: (a) three-dimensional visualization including isosurfaces of $\hat{Q}D^2/U_\infty^2 = 500$ and (b) bi-dimensional visualization including isolines of $\hat{c}_p = -1.0$. *F* and *R* indicating the signatures of the vortex ring lobes originating from the front and rear propellers, respectively.
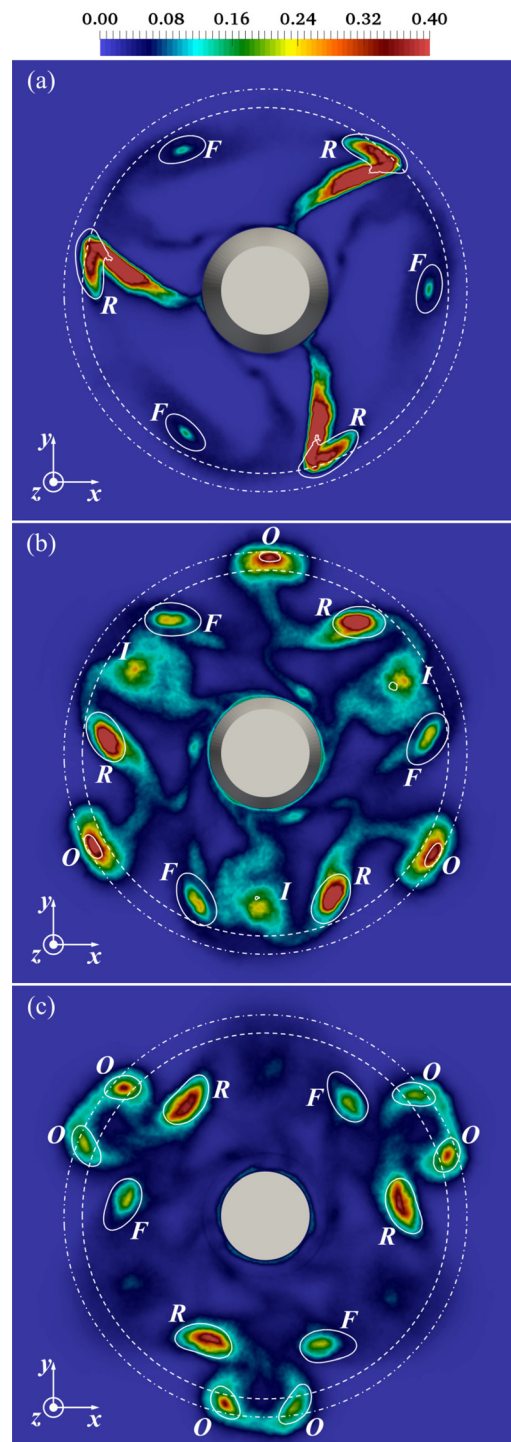
FIG. 20. Contours of phase-averaged turbulent kinetic energy, scaled by U_∞^2, in the wake of *CRP* on cross-stream slices of streamwise coordinates (a) $z/D = 0.45$, (b) $z/D = 0.85$, and (c) $z/D = 1.10$. Isolines of phase-averaged pressure coefficient $\hat{c}_p = -1.0$. *F* and *R* indicating the signatures of the vortex ring lobes originating from the front and rear propellers, respectively. *O* and *I* indicating the signatures of the outward and inward U-shaped vortex lobes, respectively.
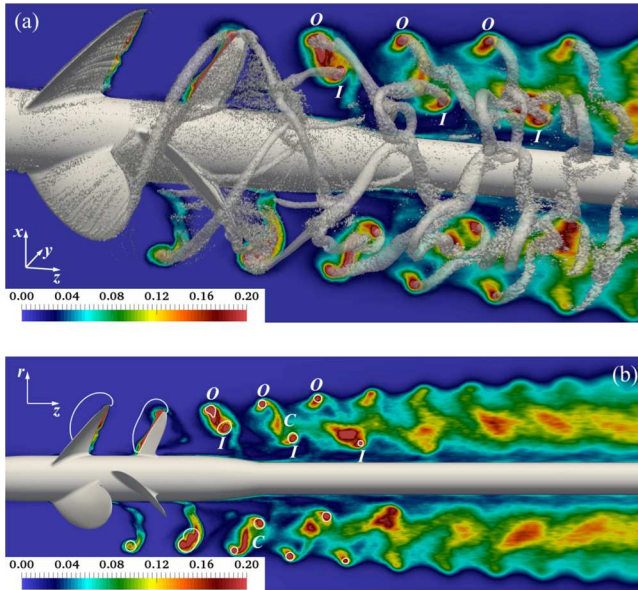
08 May 2024 09:22:52

FIG. 21. Contours of phase-averaged turbulent kinetic energy, scaled by U_∞^2, in the wake of *CRP* on a meridian slice cutting the outward and inward vortex lobes connecting the helical lobes of the vortex rings: (a) three-dimensional visualization including isosurfaces of $\hat{Q}D^2/U_\infty^2 = 500$ and (b) bi-dimensional visualization including isolines of $\hat{c}_p = -1.0$. *O* and *I* indicating the signatures of the outward and inward U-shaped vortex lobes, respectively. *C* indicating the signature of the radial structures connecting the outward and inward lobes of the vortex rings during the early stages after their onset.

turbulent kinetic energy, caused by the breakup of the tip vortices. This is already the case at about $z/D = 2.0$, in agreement with the radial profiles of Fig. 24.

F. Ensemble-averaged turbulent shear stresses

The substantial increase in the $\overline{u'w'}$ shear stresses in the wake of *CRP*, reflected in the increase in turbulent kinetic energy, is shown in Fig. 27, where ensemble-averaged contours are reported. This is the shear stress contributing the most to turbulent production, which is given by $-\overline{u_i'u_j'}\,\partial\overline{u}_i/\partial x_j$, since the largest gradients are those affecting the streamwise velocity along the radial direction, especially at the wake boundary. Therefore, the leading term of turbulent production in the cylindrical reference frame is $-\overline{u'w'}\,\partial\overline{w}/\partial r$.

The maxima of $\overline{u'w'}$ achieved at the outer boundary of the wake are significantly higher downstream of *CRP*, compared to the two isolated propellers, as a result of the shear between the tip vortices shed by the front and rear propellers. Also, in Fig. 27(a), the onset of an additional, lower peak is distinguishable, diverging downstream toward outer radial coordinates, again as a result of the outward shift of the upstream vortex lobes of the vortex rings of the *CRP* wake. The contours in the wake of the two isolated propellers are very different. The near wake is characterized by substantially lower levels of turbulent shear stress and an increase is produced only further downstream, due to the instability of the tip vortices. This instability is reflected in Figs. 27(b) and 27(c) in the radial diffusion of the maxima at the outer boundary of the wake, as it develops downstream.
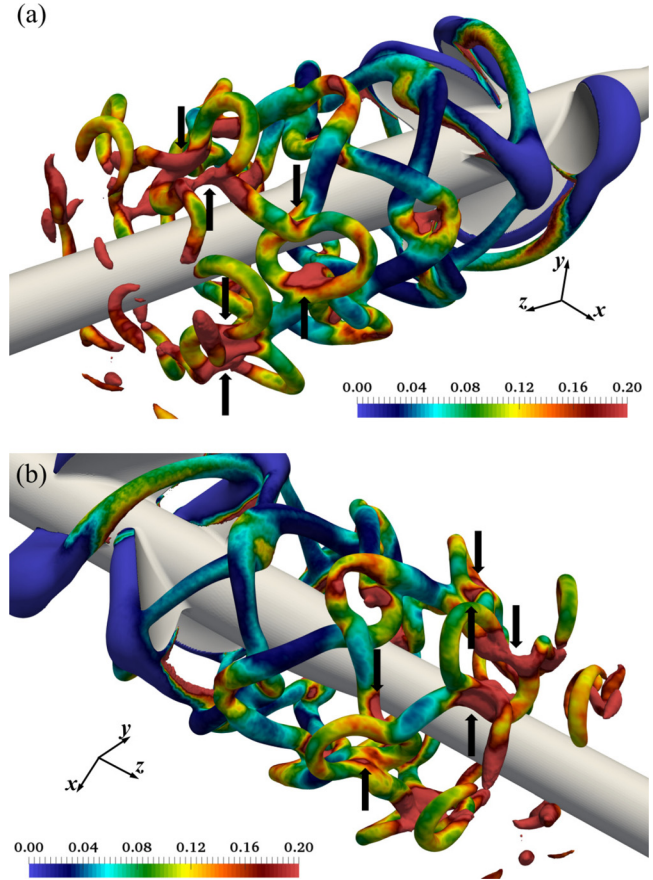

FIG. 22. Isosurfaces of phase-averaged pressure coefficient ($\hat{c}_p = -1.0$), colored by phase-averaged turbulent kinetic energy, scaled by U_∞^2. Different views in (a) and (b). Arrows indicating the areas of the highest turbulence, due to the shear between neighboring vortex rings.

In the near wake, the contours of Fig. 27(a) are actually saturated for visibility of more wake features at downstream coordinates. Therefore, more detailed comparisons are made available in Fig. 28, where radial profiles were extracted again at the streamwise coordinates (a) $z/D = 0.5$, (b) $z/D = 1.0$, and (c) $z/D = 2.0$. It is clear that the production of turbulence is substantially enhanced by the increased shear stresses when the tip vortices of the two propellers interact with each other. This is the case across all streamwise coordinates in the near wake, as demonstrated in Fig. 29, where the streamwise evolution of the peak at the outer boundary of the wake is reported: the values for *CRP* are an order of magnitude higher than those associated with the tip vortices shed by the two propellers working alone. In agreement with the behavior observed for the normal stresses of turbulence, local maxima and minima are produced by the interplay between the tip vortices coming from the front and rear propellers, as long as they keep coherent, up to about $z/D = 2.0$. At this streamwise location, a lower, broader maximum is the result of the breakup of the coherence of the vortices populating the outer boundary of the wake, as also illustrated in Fig. 27(a).
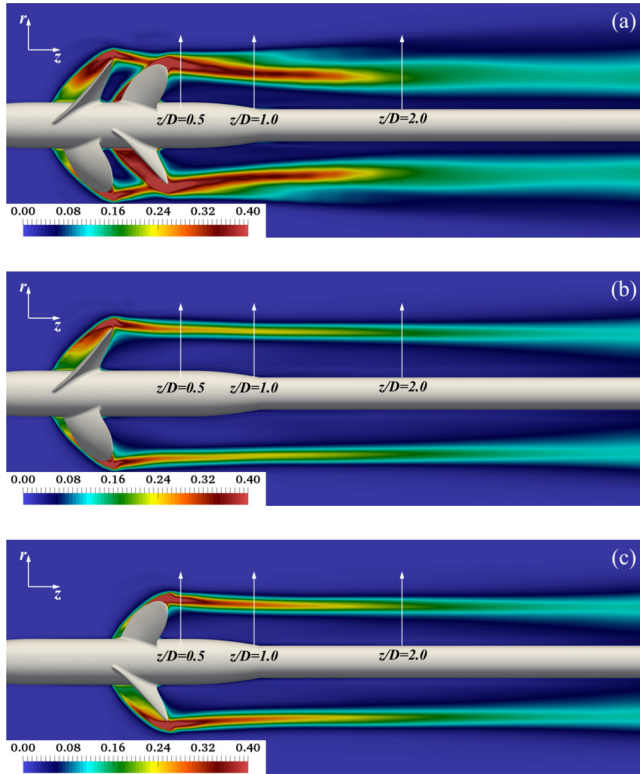
FIG. 23. Ensemble-averaged contours of turbulent kinetic energy, scaled by U_∞^2, on a meridian slice: (a) *CRP*; (b) *FRONT*; and (c) *REAR*.

The substantial modification of the flow physics in the wake of *CRP* is also demonstrated by the turbulent shear stress $\overline{v'w'}$ in Fig. 30. Downstream of the two isolated propellers the signature of their tip vortices is characterized by a couple of strong positive and negative peaks of this stress, as long as they keep coherent. The topology of the contours for *CRP* is significantly modified and in this case lower levels are achieved, in contrast with the behavior found for $\overline{u'w'}$. This is also shown through the radial profiles of Fig. 31 and the streamwise evolution of its peak value in Fig. 32. Dealing with Fig. 32, it should be noted that the result for *CRP* is affected by the lack of a sharp, dominant peak of $\overline{v'w'}$ across the near wake, in contrast with the cases of the two isolated propellers. The peak value of $\overline{v'w'}$ in the wake of the rear propeller is actually negative; therefore, in Fig. 32, its sign was switched for visualization purposes. It is worth mentioning that also the turbulent shear stress $\overline{u'v'}$ was computed, but for limitation of space it is not reported, since it was found significantly lower than both $\overline{u'w'}$ and $\overline{v'w'}$ for both propellers working alone and together.

Also for the turbulent shear stresses grid convergence was verified, as shown in Fig. 33, where radial profiles for $\overline{u'w'}$ and $\overline{v'w'}$ are reported at the streamwise coordinate $z/D = 1.0$. The results for $\overline{u'w'}$ almost overlap across grids. A small grid-dependence is observed for $\overline{v'w'}$, with some deviations of the profiles from the computations on the coarse grid, while those on the medium and fine grids display again a close agreement.
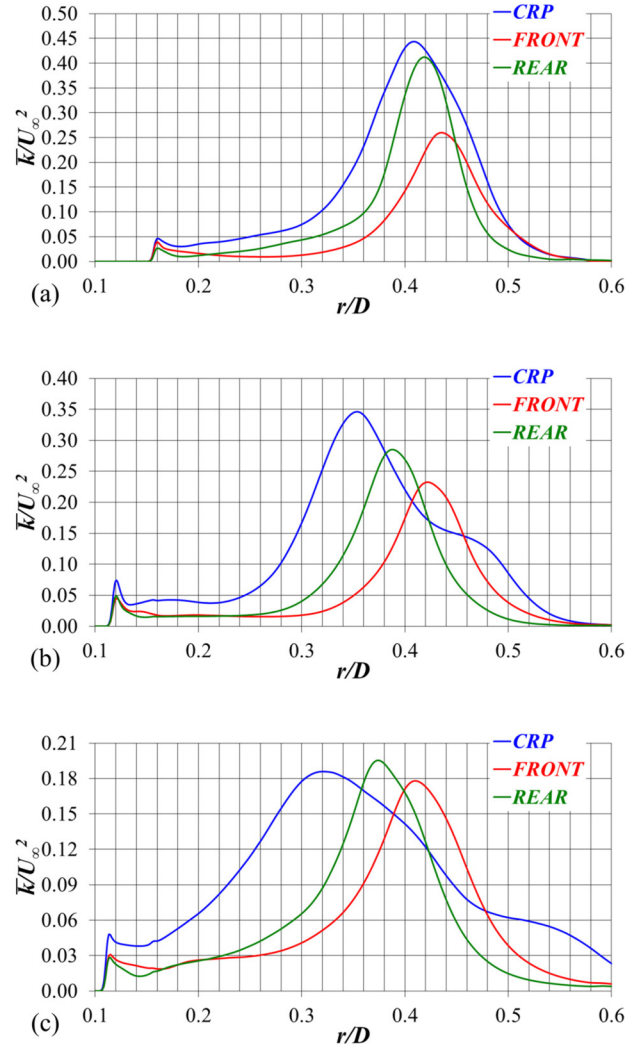

FIG. 24. Radial profiles of ensemble-averaged turbulent kinetic energy at the streamwise locations indicated by arrows in Fig. 23: (a) $z/D = 0.5$; (b) $z/D = 1.0$; and (c) $z/D = 2.0$.
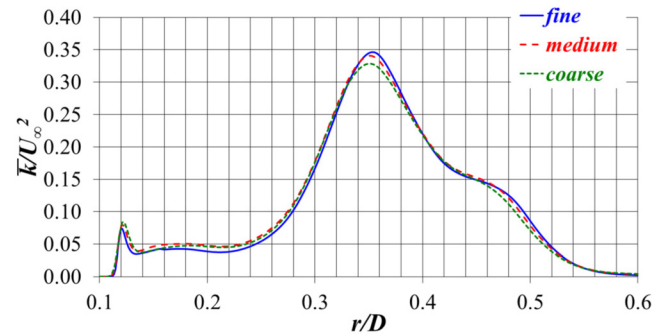

FIG. 25. Radial profiles of ensemble-averaged turbulent kinetic energy at the streamwise location $z/D = 1.0$ from the computations dealing with the *CRP* system on the fine, medium, and coarse grids.
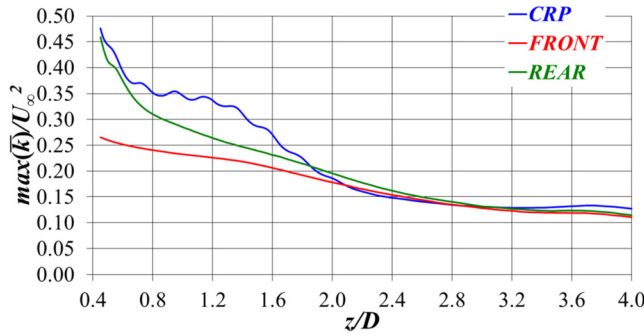
FIG. 26. Streamwise evolution of the peak of ensemble-averaged turbulent kinetic energy at the outer boundary of the wake from the data in Fig. 23.

VI. CONCLUSIONS

Large eddy simulation was adopted to reproduce the wake flow generated by two contra-rotating propellers, including the interaction between the helical tip vortices shed by each of them. Comparisons with experiments were reported, finding an excellent agreement with them on both the performance of the propellers and the intricate topology of the wake structures, but providing a higher level of detail, thanks to the availability of the full three-dimensional flow field in the near wake across a wider domain. Also, the two propellers working
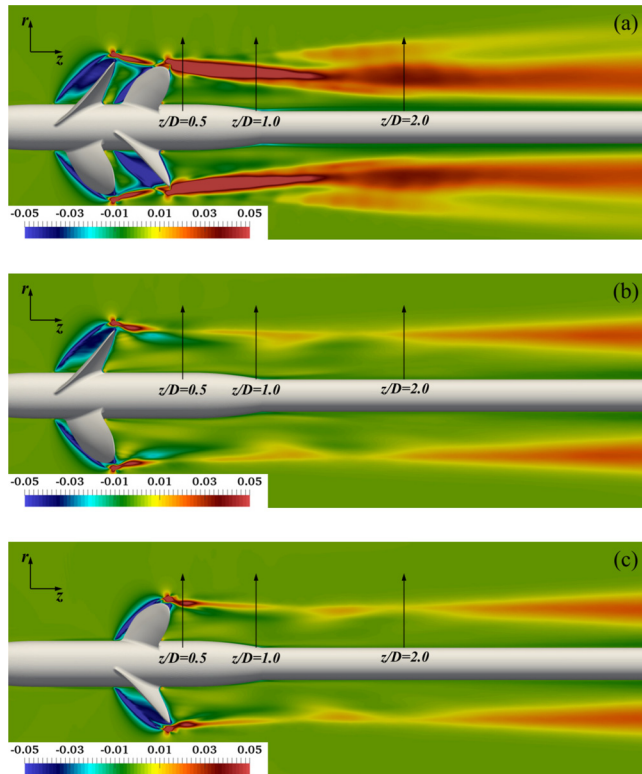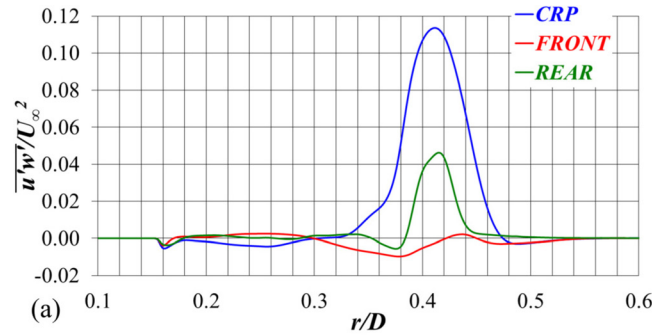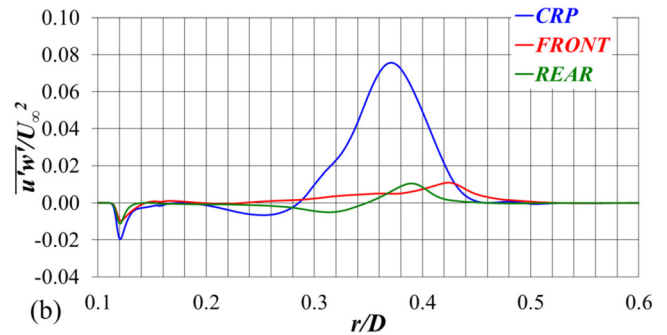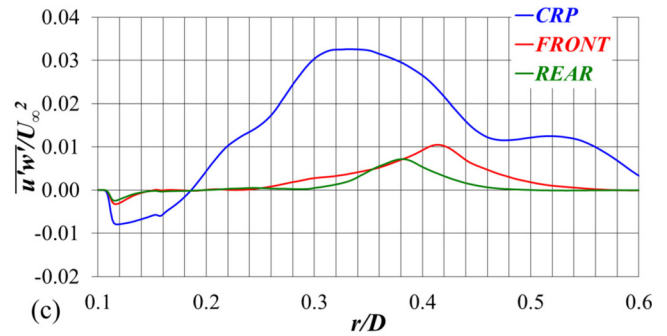

FIG. 27. Ensemble-averaged contours of the turbulent shear stress $\overline{u'w'}$, scaled by U_∞^2, on a meridian slice: (a) CRP; (b) FRONT; and (c) REAR.

FIG. 28. Radial profiles of ensemble-averaged turbulent shear stress $\overline{u'w'}$ at the streamwise locations indicated by arrows in Fig. 27: (a) $z/D = 0.5$; (b) $z/D = 1.0$; and (c) $z/D = 2.0$.

alone were simulated, for comparison purposes, helping us to identify the effect of the interaction between them in the contra-rotating system on both performance and the wake dynamics.

The interaction between the helical tip vortices results in the onset of vortex rings consisting of six helical vortex lobes. These lobes come alternatively from the front and rear propellers, respectively. They are linked by three upstream and three downstream U-shaped vortex lobes. They experience a shift toward outer and inner radial coordinates, respectively. This shift is due to the shear with the upstream and downstream vortex rings, respectively. The regions of shear between the legs of the outward and inward vortex lobes of consecutive vortex rings are characterized by the highest turbulent stresses. The six helical lobes of each vortex ring also differ for the levels of
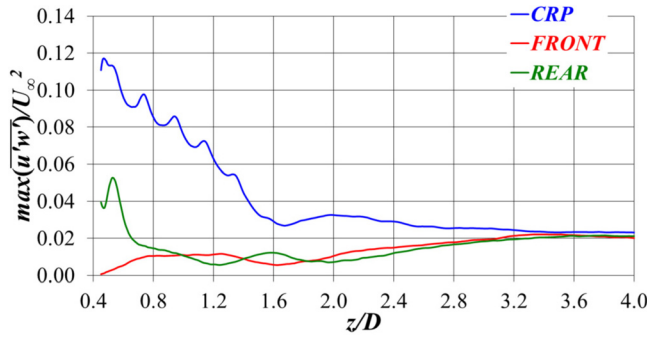
FIG. 29. Streamwise evolution of the peak of ensemble-averaged turbulent shear stress $\overline{u'w'}$ at the outer boundary of the wake from the data in Fig. 27.

turbulence at their core. Higher turbulent stresses occur in the lobes originating from the tip vortices of the rear propeller, compared to those in the lobes from the tip vortices of the front propeller: the rear propeller, ingesting the turbulent wake of the front propeller, sheds tip vortices characterized by higher levels of turbulent kinetic energy at their core.

The outward projection of the upstream U-shaped vortex lobes produces an expansion of the wake. This is in contrast with the typical contraction of the wake of isolated propellers, as also shown by the
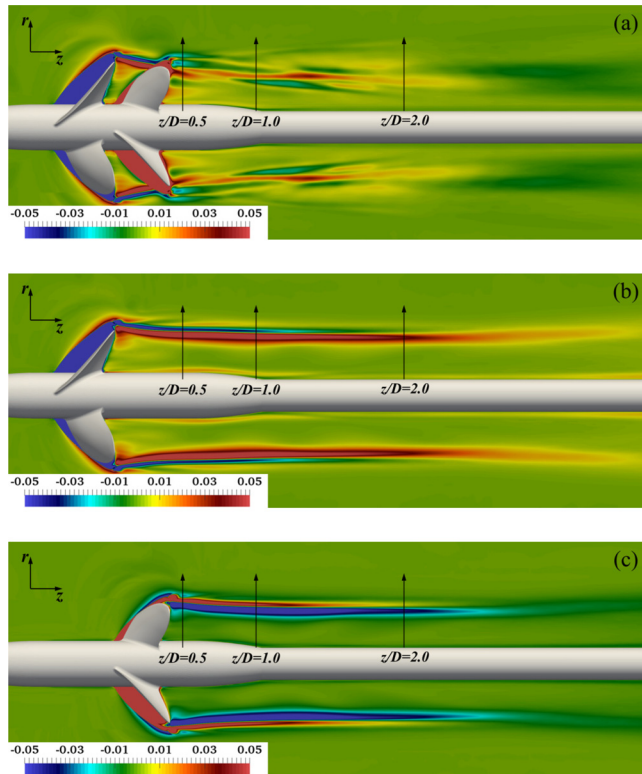

FIG. 30. Ensemble-averaged contours of the turbulent shear stress $\overline{v'w'}$, scaled by U_∞^2, on a meridian slice: (a) CRP; (b) FRONT; and (c) REAR.
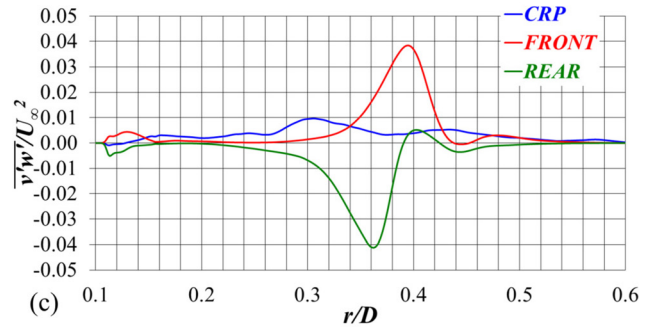

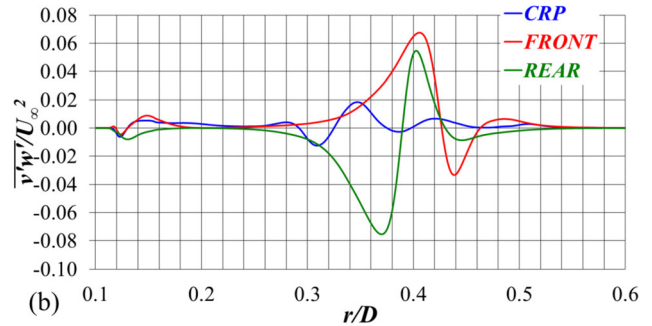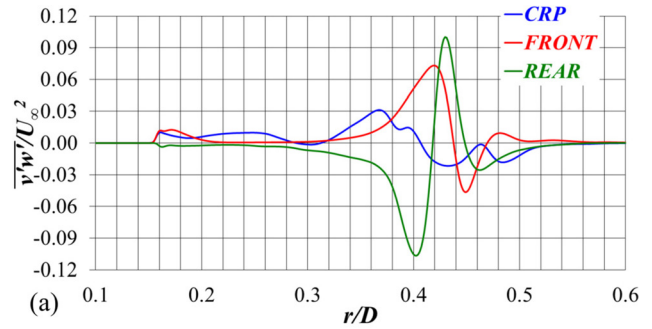**FIG. 31.** Radial profiles of ensemble-averaged turbulent shear stress $\overline{v'w'}$ at the streamwise locations indicated by arrows in Fig. 30: (a) $z/D = 0.5$; (b) $z/D = 1.0$; and (c) $z/D = 2.0$.
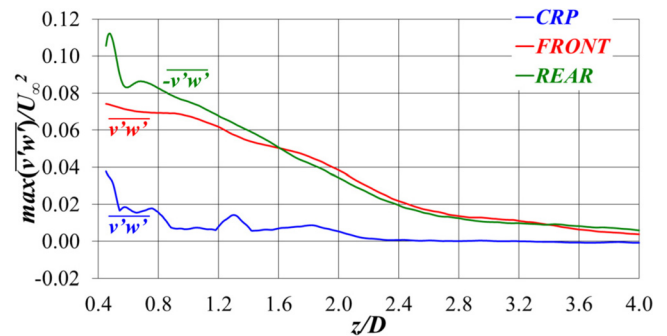

FIG. 32. Streamwise evolution of the peak of ensemble-averaged turbulent shear stress $\overline{v'w'}$ at the outer boundary of the wake from the data in Fig. 30.
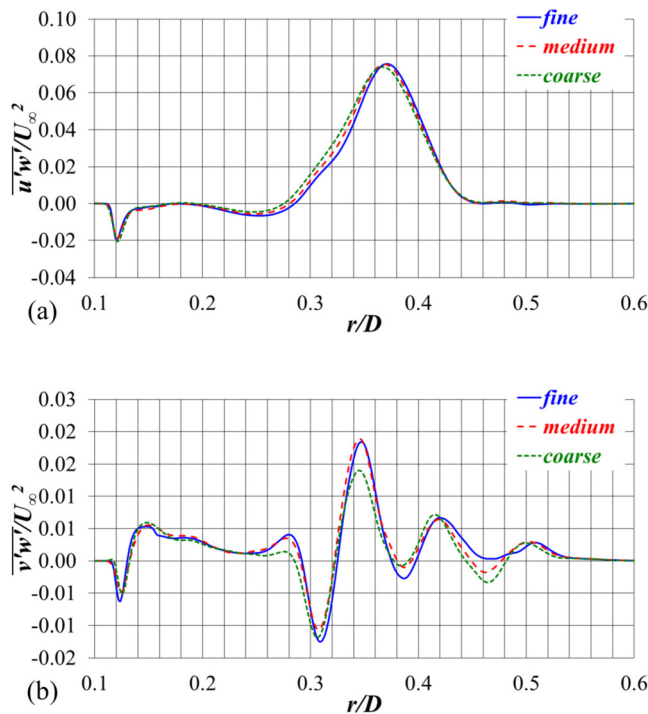
08 May 2024 09:22:52

FIG. 33. Radial profiles of ensemble-averaged turbulent shear stresses (a) $\overline{u'w'}$ and (b) $\overline{v'w'}$ at the streamwise location $z/D = 1.0$ from the computations dealing with the *CRP* system on the fine, medium and coarse grids.

comparison with the wakes of the front and rear propellers working alone. This comparison also revealed a significant increase in the levels of turbulence in the region of the wake populated by the tip vortices and a faster break up of their coherence, due to the shear developed between them. In addition, the monotonic evolution of turbulence at the outer boundary of the wake is replaced by local maxima and minima, as long as the coherence of the wake structures is not disrupted by instability phenomena. This behavior was found associated with the turbulent shear stress involving the radial and streamwise velocity components, which is the major source of turbulence production at the outer boundary of the wake.

AUTHOR DECLARATIONS
Conflict of Interest

The authors have no conflicts to disclose.

Author Contributions

Antonio Posa: Conceptualization (equal); Data curation (lead); Formal analysis (lead); Investigation (lead); Methodology (lead); Resources (lead); Software (lead); Supervision (lead); Validation (lead); Visualization (lead); Writing – original draft (lead); Writing – review & editing (lead). **Alessandro Capone:** Conceptualization (equal); Data curation (supporting); Formal analysis (supporting); Investigation (supporting); Supervision (supporting); Validation (supporting); Visualization (supporting); Writing – original draft (supporting); Writing – review & editing (supporting). **Francisco Alves Pereira:** Conceptualization (equal); Data curation (supporting); Formal analysis (supporting); Funding acquisition (lead); Investigation (supporting); Project administration (lead); Validation (supporting); Writing – original draft (supporting); Writing – review & editing (supporting). **Fabio Di Felice:** Conceptualization (equal); Data curation (supporting); Formal analysis (supporting); Funding acquisition (lead); Investigation (supporting); Project administration (lead); Validation (supporting); Writing – original draft (supporting); Writing – review & editing (supporting). **Riccardo Broglia:** Conceptualization (equal); Formal analysis (supporting); Investigation (supporting); Resources (supporting); Supervision (supporting); Writing – original draft (supporting); Writing – review & editing (supporting).

DATA AVAILABILITY

The data that support the findings of this study are available from the corresponding author upon reasonable request.

REFERENCES

[1] K.-S. Min, B.-J. Chang, and H.-W. Seo, "Study on the contra-rotating propeller system design and full-scale performance prediction method," Int. J. Nav. Archit. Ocean Eng. **1**, 29–38 (2009).

[2] D. Grassi, S. Brizzolara, M. Viviani, L. Savio, and S. Caviglia, "Design and analysis of counter-rotating propellers-comparison of numerical and experimental results," J. Hydrodyn. **22**, 553–576 (2010).

[3] B.-J. Chang and S. Go, "Study on a procedure for propulsive performance prediction for CRP-POD systems," J. Mar. Sci. Technol. **16**, 1–7 (2011).

[4] Y. Xiong, K. Zhang, Z-z Wang, and W-j Qi, "Numerical and experimental studies on the effect of axial spacing on hydrodynamic performance of the hybrid CRP pod propulsion system," China Ocean Eng. **30**, 627–636 (2016).

[5] Y. Su, S. A. Kinnas, and H. Jukola, "Application of a BEM/RANS interactive method to contra-rotating propellers," in *Proceedings of the Fifth International Symposium on Marine Propulsion*, Espoo, Finland, 2017.

[6] Y. Su and S. A. Kinnas, "A BEM/RANS interactive method for predicting contra-rotating propeller performance," Ocean Syst. Eng. **7**, 329–344 (2017).

[7] M. R. Khan, R. Kundu, W. Rahman, M. M. Haque, and M. R. Ullah, "Efficiency study: Contra-rotating propeller system," AIP Conf. Proc. **1980**, 060001 (2018).

[8] N. M. Nouri, S. Mohammadi, and M. Zarezadeh, "Optimization of a marine contra-rotating propellers set," Ocean Eng. **167**, 397–404 (2018).

[9] Y.-S. Huang, X.-Q. Dong, C.-J. Yang, W. Li, and F. Noblesse, "Design of wake-adapted contra-rotating propellers for high-speed underwater vehicles," Appl. Ocean Res. **91**, 101880 (2019).

[10] L. Hou, L. Yin, A. Hu, X. Chang, Y. Lin, and S. Wang, "Optimal matching investigation of marine contra-rotating propellers for energy consumption minimization," J. Mar. Sci. Technol. **26**, 1184–1197 (2021).

[11] M. Tadros, M. Ventura, and C. Guedes Soares, "Towards fuel consumption reduction based on the optimum contra-rotating propeller," J. Mar. Sci. Eng. **10**, 1657 (2022).

[12] M. Felli, R. Camussi, and F. Di Felice, "Mechanisms of evolution of the propeller wake in the transition and far fields," J. Fluid Mech. **682**, 5–53 (2011).

[13] E. Balaras, S. Schroeder, and A. Posa, "Large-eddy simulations of submarine propellers," J. Ship Res. **59**, 227–237 (2015).

[14] P. Kumar and K. Mahesh, "Large eddy simulation of propeller wake instabilities," J. Fluid Mech. **814**, 361–396 (2017).

[15] A. Posa, R. Broglia, M. Felli, M. Falchi, and E. Balaras, "Characterization of the wake of a submarine propeller via Large-Eddy simulation," Comput. Fluids **184**, 138–152 (2019).

[16] S. Ahmed, P. Croaker, and C. J. Doolan, "On the instability mechanisms of ship propeller wakes," Ocean Eng. **213**, 107609 (2020).

[17] L. Wang, T. Wu, J. Gong, and Y. Yang, "Numerical simulation of the wake instabilities of a propeller," Phys. Fluids **33**, 125125 (2021).

[18] L. Wang, X. Liu, N. Wang, and M. Li, "Modal analysis of propeller wakes under different loading conditions," Phys. Fluids **34**, 065136 (2022a).

[19] C. Wang, P. Li, C. Guo, L. Wang, and S. Sun, "Numerical research on the instabilities of CLT propeller wake," Ocean Eng. **243**, 110305 (2022b).

[20] A. Posa, "The dynamics of the tip vortices shed by a tip-loaded propeller with winglets," J. Fluid Mech. **951**, A25 (2022a).

[21] C. Sun and L. Wang, "Modal analysis of propeller wake dynamics under different inflow conditions," Phys. Fluids **34**, 125109 (2022).

[22] A. Posa, "Anisotropy of turbulence at the core of the tip and hub vortices shed by a marine propeller," J. Fluid Mech. **969**, A23 (2023a).

[23] L. Wang, X. Liu, J. Guo, M. Li, and J. Liao, "The dynamic characteristics in the wake systems of a propeller operating under different loading conditions," Ocean Eng. **286**, 115518 (2023a).

[24] A. Capone and F. Alves Pereira, "Unraveling the interplay of two counter-rotating helical vortices," Phys. Rev. Fluids **5**, 110509 (2020).

[25] A. Capone, F. Di Felice, and F. Alves Pereira, "On the flow field induced by two counter-rotating propellers at varying load conditions," Ocean Eng. **221**, 108322 (2021).

[26] F. Alves Pereira, A. Capone, and F. Di Felice, "Flow field and vortex interactions in the near wake of two counter-rotating propellers," Appl. Ocean Res. **117**, 102916 (2021).

[27] K.-J. Paik, S. Hwang, J. Jung, T. Lee, Y.-Y. Lee, H. Ahn, and S.-H. Van, "Investigation on the wake evolution of contra-rotating propeller using RANS computation and SPIV measurement," Int. J. Nav. Archit. Ocean Eng. **7**, 595–609 (2015).

[28] Y.-S. Huang, J. Yang, and C.-J. Yang, "Numerical prediction of the effective wake profiles of a high-speed underwater vehicle with contra-rotating propellers," Appl. Ocean Res. **84**, 242–249 (2019).

[29] Y.-X. Zhang, X.-P. Wu, Z.-Y. Zhou, X.-K. Cheng, and Y.-L. Li, "A numerical study on the interaction between forward and aft propellers of hybrid CRP pod propulsion systems," Ocean Eng. **186**, 106084 (2019).

[30] J. Hu, Y. Wang, W. Zhang, X. Chang, and W. Zhao, "Tip vortex prediction for contra-rotating propeller using large eddy simulation," Ocean Eng. **194**, 106410 (2019).

[31] J. Hu, X. Ning, W. Zhao, F. Li, J. Ma, W. Zhang, S. Sun, M. Zou, and C. Lin, "Numerical simulation of the cavitating noise of contra-rotating propellers based on detached eddy simulation and the Ffowcs Williams-Hawkings acoustics equation," Phys. Fluids **33**, 115117 (2021).

[32] M. Felli, R. Camussi, and G. Guj, "Experimental analysis of the flow field around a propeller-rudder configuration," Exp. Fluids **46**, 147–164 (2009).

[33] M. Felli and M. Falchi, "Propeller tip and hub vortex dynamics in the interaction with a rudder," Exp. Fluids **51**, 1385–1402 (2011).

[34] J. Hu, W. Zhang, S. Sun, and C. Guo, "Numerical simulation of vortex–rudder interactions behind the propeller," Ocean Eng. **190**, 106446 (2019b).

[35] L. Wang, C. Guo, P. Xu, and Y. Su, "Analysis of the wake dynamics of a propeller operating before a rudder," Ocean Eng. **188**, 106250 (2019).

[36] J. Hu, W. Zhang, H. Guo, S. Sun, F. Chen, and C. Guo, "Numerical simulation of propeller wake vortex–rudder interaction in oblique flows," Ships Offshore Struct. **16**, 144–155 (2021b).

[37] A. Posa and R. Broglia, "Spanwise distribution of the loads on a hydrofoil working in the wake of an upstream propeller," Ocean Eng. **264**, 112542 (2022a).

[38] A. Posa and R. Broglia, "Near wake of a propeller across a hydrofoil at incidence," Phys. Fluids **34**, 065141 (2022).

[39] A. Posa, "Tip vortices shed by a hydrofoil in the wake of a marine propeller," Phys. Fluids **34**, 125134 (2022).

[40] A. Posa, "End effects in the wake of a hydrofoil working downstream of a propeller," Phys. Fluids **35**, 045122 (2023).

[41] J. Bosschers, "A semi-empirical prediction method for broadband hull-pressure fluctuations and underwater radiated noise by propeller tip vortex cavitation," J. Mar. Sci. Eng. **6**, 49 (2018).

[42] G. Ku, J. Cho, C. Cheong, and H. Seol, "Numerical investigation of tip-vortex cavitation noise of submarine propellers using hybrid computational hydroacoustic approach," Ocean Eng. **238**, 109693 (2021).

[43] A. Posa, R. Broglia, M. Felli, M. Cianferra, and V. Armenio, "Hydroacoustic analysis of a marine propeller using large-eddy simulation and acoustic analogy," J. Fluid Mech. **947**, A46 (2022).

[44] S. Sezen and M. Atlar, "Numerical investigation into the effects of tip vortex cavitation on propeller underwater radiated noise (URN) using a hybrid CFD method," Ocean Eng. **266**, 112658 (2022).

[45] A. Posa, "Comparison between the acoustic signatures of a conventional propeller and a tip-loaded propeller with winglets," Phys. Fluids **35**, 025133 (2023c).

[46] A. Posa and R. Broglia, "Influence of the load conditions on the acoustic signature of a tip-loaded propeller with winglets," Phys. Fluids **35**, 045147 (2023).

[47] X. Wang, X. Bai, H. Cheng, B. Ji, and X. Peng, "Numerical investigation of cavitating tip vortex dynamics and how they influence the acoustic characteristics," Phys. Fluids **35**, 062119 (2023).

[48] V. Okulov, "On the stability of multiple helical vortices," J. Fluid Mech. **521**, 319–342 (2004).

[49] V. Okulov and J. Sørensen, "Stability of helical tip vortices in a rotor far wake," J. Fluid Mech. **576**, 1–25 (2007).

[50] T. Leweke, H. Quaranta, H. Bolnot, F. Blanco-Rodríguez, and S. L. Dizès, "Long- and short-wave instabilities in helical vortices," J. Phys: Conf. Ser. **524**, 012154 (2014).

[51] I. Delbende, B. Piton, and M. Rossi, "Merging of two helical vortices," Eur. J. Mech. B **49**, 363–372 (2015).

[52] F. J. Blanco-Rodríguez, S. Le Dizès, C. Selçuk, I. Delbende, and M. Rossi, "Internal structure of vortex rings and helical vortices," J. Fluid Mech. **785**, 219–247 (2015).

[53] C. Selçuk, I. Delbende, and M. Rossi, "Helical vortices: Linear stability analysis and nonlinear dynamics," Fluid Dyn. Res. **50**, 011411 (2018).

[54] H. U. Quaranta, M. Brynjell-Rahkola, T. Leweke, and D. S. Henningson, "Local and global pairing instabilities of two interlaced helical vortices," J. Fluid Mech. **863**, 927–955 (2019).

[55] I. Delbende, C. Selçuk, and M. Rossi, "Nonlinear dynamics of two helical vortices: A dynamical system approach," Phys. Rev. Fluids **6**, 084701 (2021).

[56] A. Abraham, A. Castillo-Castellanos, and T. Leweke, "Simplified model for helical vortex dynamics in the wake of an asymmetric rotor," Flow **3**, E5 (2023).

[57] F. Nicoud and F. Ducros, "Subgrid-scale stress modelling based on the square of the velocity gradient tensor," Flow, Turbul., Combust. **62**, 183–200 (1999).

[58] A. Posa, "Dependence of tip and hub vortices shed by a propeller with winglets on its load conditions," Phys. Fluids **34**, 105107 (2022c).

[59] A. Posa and R. Broglia, "Influence by the hub vortex on the instability of the tip vortices shed by propellers with and without winglets," Phys. Fluids **34**, 115115 (2022c).

[60] E. Balaras, "Modeling complex boundaries using an external force field on fixed Cartesian grids in large-eddy simulations," Comput. Fluids **33**, 375–404 (2004).

[61] J. Yang and E. Balaras, "An embedded-boundary formulation for large-eddy simulation of turbulent flows interacting with moving boundaries," J. Comput. Phys. **215**, 12–40 (2006).

[62] J. Van Kan, "A second-order accurate pressure-correction scheme for viscous incompressible flow," SIAM J. Sci. Stat. Comput. **7**, 870–891 (1986).

[63] T. Rossi and J. Toivanen, "A parallel fast direct solver for block tridiagonal systems with separable matrices of arbitrary dimension," SIAM J. Sci. Comput. **20**, 1778–1793 (1999).

[64] J. Jeong and F. Hussain, "On the identification of a vortex," J. Fluid Mech. **285**, 69–94 (1995).

08 May 2024 09:22:52